SANDIA REPORT
SAND2019-11868
Printed September 2019

Sandia National Laboratories

X-ray diffraction of dynamically compressed matter on Sandia's Z Pulsed Power Facility

T. Ao, M. S. Schollmeier, P. Kalita, P. D. Gard, J. R. Williams, C. B. Blada, H. L. Hanshaw, I. C. Smith, J. E. Shores, C. S. Speas, and C. T. Seagle

Prepared by
Sandia National Laboratories
Albuquerque, New Mexico
87185 and Livermore,
California 94550

Issued by Sandia National Laboratories, operated for the United States Department of Energy by National Technology & Engineering Solutions of Sandia, LLC.

Available to DOE and DOE contractors from
U.S. Department of Energy
Office of Scientific and Technical Information
P.O. Box 62
Oak Ridge, TN 37831

Telephone: (865) 576-8401
Facsimile: (865) 576-5728
E-Mail: reports@osti.gov
Online ordering: http://www.osti.gov/scitech

Available to the public from
U.S. Department of Commerce
National Technical Information Service
5301 Shawnee Rd
Alexandria, VA 22312

Telephone: (800) 553-6847
Facsimile: (703) 605-6900
E-Mail: orders@ntis.gov
Online order: https://classic.ntis.gov/help/order-methods/

ABSTRACT

Sandia's Z Pulsed Power Facility is able to dynamically compress matter to extreme states with exceptional uniformity, duration, and size, which are ideal for investigations of fundamental material properties of high energy density conditions. X-ray diffraction (XRD) is a key atomic scale probe since it provides direct observation of the compression and strain of the crystal lattice, and is used to detect, identify, and quantify phase transitions. Because of the destructive nature of Z-Dynamic Materials Properties (DMP) experiments and low signal vs background emission levels of XRD, it is very challenging to detect the XRD pattern close to the Z-DMP load and to recover the data. We developed a new Spherical Crystal Diffraction Imager (SCDI) diagnostic to relay and image the diffracted x-ray pattern away from the load debris field. The SCDI diagnostic utilizes the Z-Beamlet laser to generate 6.2-keV Mn-He_{α} x-rays to probe a shock-compressed sample on the Z-DMP load. A spherically bent crystal composed of highly oriented pyrolytic graphite is used to collect and focus the diffracted x-rays into a 1-inch thick tungsten housing, where an image plate is used to record the data. We performed experiments to implement the SCDI diagnostic on Z to measure the XRD pattern of shock compressed beryllium samples at pressures of 1.8-2.2 Mbar.

ACKNOWLEDGMENTS

The authors would like to acknowledge the large teams at Sandia's Z Pulsed Power and Z-Backlighter Laser Facilities that contributed to the design, fabrication, and fielding of the complex Z experiments.

CONTENTS

LIST OF FIGURES

LIST OF TABLES

This page left blank

ACRONYMS AND DEFINITIONS

Abbreviation	Definition
A-K	Anode-Cathode
bcc	Body centered cubic
Be	Beryllium
DISCO	Diffraction scintillator optic
DMP	Dynamic Material Properties
EMP	Electromagnetic pulse
EOS	Equation-of-state
FOA	Final optics assembly
FWHM	Full-Width-at-Half-Maximum
hcp	Hexagonal close packed
HED	High Energy Density
hkl	Miller indices
High-Z	High atomic number
HOPG	Highly oriented pyrolytic graphite
IP	Image plate
LDA	Linear array diode
Low-Z	Low atomic number
Mn	Manganese
PDV	Photonic Doppler Velocimetry
SCDI	Spherical Crystal Diffraction Imager
SMASH	Sandia Matlab AnalysiS Hierarchy
UXI	Ultrafast X-ray Imager
VISAR	Velocity Interferometer System for Any Reflector
XPL	X-ray polycapillary lens
XRD	X-ray diffraction
Z	Z-accelerator
ZBL	Z-Beamlet
ZPW	Z-Petawatt

1. INTRODUCTION

1.1. Z-accelerator for HED research

High Energy Density (HED) physics refers to the study of states with energy densities exceeding 10^{11} J/m^3, which exists in the cores of planets and stars, during intense shock loading of materials, and during the implosion of inertial confinement fusion capsules. Such concentrated amounts of energy correspond to states under extreme pressures, which are challenging to describe theoretically and investigate experimentally. The Sandia Z-accelerator is a large pulsed-power facility (~30 m in diameter), which can generate a shaped electrical pulse with highly controllable rise time (100–1200 ns) and peak current up to 26 MA [1]. Over the last two decades, Z has been used, in a so-called Dynamic Material Properties (DMP) configuration, to extensively collect information on the high-pressure equation-of-states (EOS) of materials. Specifically, numerous shock compression experiments on Z have examined the response of materials along their principal Hugoniots, which produce higher temperature states at given compressions ([2], [3], [4], [5], [6], [7]). Other Z experiments have alternatively used well-controlled continuous, or ramp loading of condensed matter to obtain off-Hugoniot measurements, or cooler states at given compressions, of materials ([8], [9], [10]).

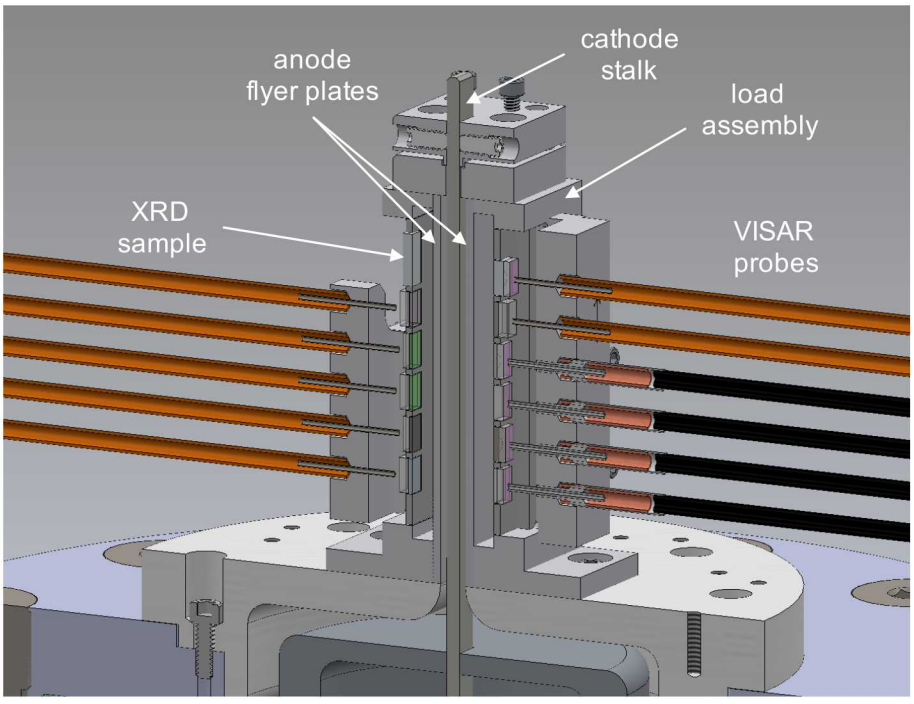

Figure 1-1. Cross-section view of Z-DMP load for the Z-XRD experiment.

In the Z-DMP shock loading configuration [7], the large currents are directed into a coaxial load consisting of two anode (north and south) plates arranged around a central cathode stalk to form two anode-cathode (A-K) vacuum gaps, as shown in Figure 1-1. A short circuit is created between the anode plates and the cathode stalk through a shorting cap at the top of the coaxial load. The current

density **J** flowing on the anode and cathode produces a planar magnetic field **B** between them, and the resulting **J×B** force produces a smooth mechanical stress wave that is proportional to the magnetic field squared. The generated impulsive pressure provides sufficient momentum to launch the anode flyer plates at high velocities across the gap toward samples located on the load assembly. Since the Z-DMP load assembly is relatively large in size (e.g. 35 mm wide, 56 mm high, 20 mm thick), it enables numerous (4–10) samples to be placed vertically along each side of the assembly that experience nearly identical impact conditions. The magnetically launched anode flyer plates may reach velocities > 30 km/s, which can shock-compress samples to pressures up to tens of Mbar.

1.2. X-ray diffraction of dynamically compressed matter

Dynamic compression experiments on Z have primarily relied upon velocimetry diagnostics, such as Velocity Interferometer System for Any Reflector (VISAR) [11] and Photonic Doppler Velocimetry (PDV) [12], to provide insight into the behavior of materials under extreme conditions at the continuum, macroscopic scale. The recent advent of XRD on gas gun impactor [13] and laser shock platforms [14] opens the door to an atomic scale understanding and quantification of shock driven processes. In fact, one of the most fundamental properties of a solid is its crystal structure. A crystalline solid is a material whose atoms are arranged in a definite, repeating pattern in three dimensions, which form a "Bravais" (crystal) lattice that extends in all directions [15]. Crystallographic planes are described using Miller indices (*hkl*), which are derived from the intercepts of the plane with the lattice. The reciprocal lattice represents the Fourier transform of the Bravais lattice that exists in real (physical) space. Analogously, the reciprocal lattice exists in reciprocal space or momentum space (also known as *k*-space). In the process of x-ray diffraction (XRD), the momentum difference between incident and diffracted x-rays of a crystal is a reciprocal lattice vector. The XRD pattern of a crystal can be used to determine the reciprocal vectors of the lattice, thus reconstructing the atomic arrangement of the crystal.

X-ray diffraction has been a key measurement in static compression diamond anvil cell experiments because it provides direct observation of the compression and strain of the crystal lattice, and is used to detect, identify, and quantify phase transitions. While XRD measurements under static pressures are routinely performed on single and polycrystalline samples, similar measurements on dynamic compression experiments are more challenging. X-ray diffraction data from shocked samples are extremely valuable as direct measurement of the elastic compression of the crystal lattice, onset of plastic flow, strength-strain rate dependence, phase transitions, and density of crystal defects such as dislocations. In-situ dynamic XRD has been performed on gas gun and laser-driven shock experiments in various forms including monochromatic Bragg reflection [16] and transmission ([13], [17]), multi-line Laue pattern [18], and time-resolved measurements ([14], [19], [20]). The dynamic responses of various materials have previously been studied with XRD on gas gun and laser facilities, including beryllium, carbon, iron, copper, zirconium, tin, bismuth, lithium fluoride, calcium fluoride, potassium chloride, and cadmium sulfide, to name a few. The development of a reliable structural and phase identification diagnostic on Z will have significant impact on Sandia's Stockpile Stewardship and National Security missions.

1.3. Challenges of implementing x-ray diffraction on Z

The Z-accelerator has several unique experimental challenges which preclude using the XRD schemes that have worked at other HED facilities, such as the OMEGA Laser Facility at the

University of Rochester [21], the National Ignition Facility at Lawrence Livermore National Laboratory [22], the Linac Coherent Light Source at SLAC National Accelerator Laboratory [23], and the Dynamic Compression Sector at the Advanced Photon Source at Argonne National Laboratory ([24], [13]). First, the samples on Z are large and thick, and the surrounding hardware consist of high-Z materials, which prevent transmission of x-rays. Thus, only a reflection geometry can be used for XRD. Second, the large current and magnetic fields of Z generate a tremendous amount of high energy photons, including MeV-scale photons near the load, which results in a very high x-ray background. Third, a very strong electromagnetic pulse (EMP) is emitted when Z fires, which could damage electronics within close range of the load or at the very least produce unwanted early triggers.

Lastly, the Z environment is very destructive. During an experiment, 22 MJ of stored electrical energy are released into the Center Section of Z, which causes the Z-DMP load to explode. Historical post-shot observations of Z-DMP experiments have shown large amounts of debris scattered throughout the load region. Figure 1-2 presents the results of an experiment (Z2959) to better examine the Z-DMP load debris field. The pre-shot image of the Z-DMP coaxial load is shown in Figure 1-2(a). A conical "witness plate" made of aluminum was placed mounted about 10 cm above the coaxial load to characterize the load debris field, as shown in Figure 1-2(b). The witness plate was severely damaged and the coaxial load was completely destroyed, as shown in the post-shot image of Figure 1-2(c). The detailed view of the deep cratering in the witness plate shown in Figure 1-2(d) provided evidence of the size and energy of debris generated from the Z-DMP load. Based on these post-shot witness plate results, direct x-ray detection and subsequent data retrieval is highly infeasible.

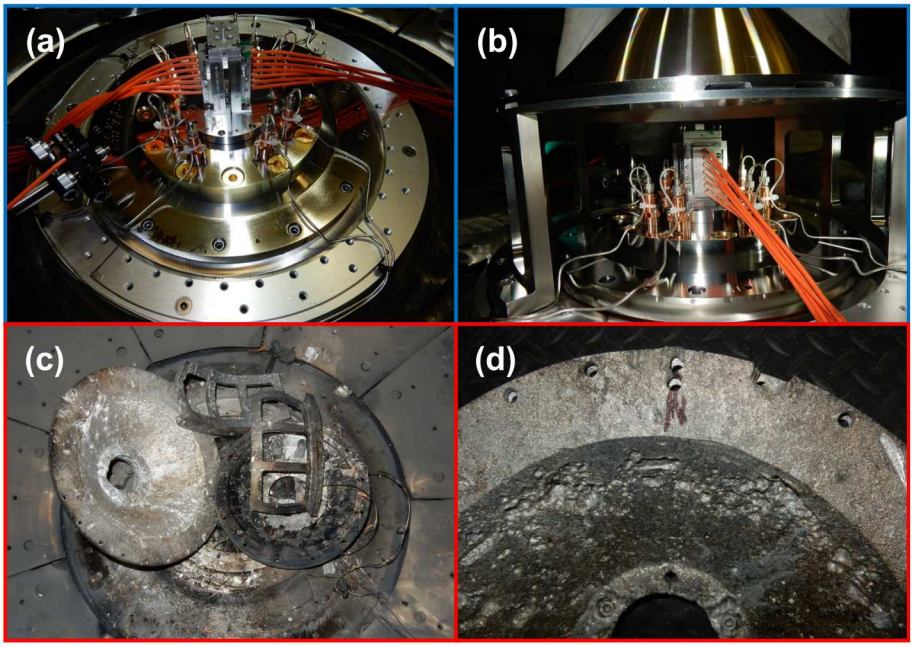

Figure 1-2. Z2959: Z-DMP experiment to characterize the load debris field within the Z Center Section. Pre-shot images of (a) coaxial load, and (b) aluminum conical debris witness plate. Post-shot images of (c) destroyed coaxial load, and (d) detailed view of debris witness plate.

1.4. Strategic plan for the Z-XRD project

The goal of this work is to develop an XRD capability for Z-DMP experiments that will enable diagnosis of the crystallographic structure and lattice parameters of shock and ramp compressed samples, while withstanding the harsh Z environment. The Z-XRD Project utilizes a 3-stage strategy to achieve its goals. In Stage 1 (near-term), XRD of compressed low-Z materials will be performed by leveraging the existing experience of spherical crystal imaging on Z. In Stage 2 (mid-term), improvements to Z-XRD will be implemented, such as increasing x-ray flux and photon energy, and time-gated x-ray detection. In Stage 3 (long-term), XRD will be incorporated with the Z-containment system to diagnose compressed special nuclear materials.

The purpose of this report is to present recent results that demonstrate the completion of the Z-XRD Project's Stage 1. Section 2 describes the spherical crystal diffraction imager (SCDI) diagnostic. The data of the Z-XRD experiments are presented and analyzed in Section 3. A brief overview of the preliminary work for the Z-XRD Project's Stages 2 and 3 is given in Section 4.

2. SPHERICAL CRYSTAL DIFFRACTION IMAGER

To overcome the challenges of implementing XRD on Z in the near-term, a new spherical crystal diffraction imager (SCDI) diagnostic has been developed. The design of the SCDI diagnostic is similar to the Z's spherical crystal x-ray backlighter diagnostic ([25], [26], [27]), since both operate as spherically bent crystal microscopes. Fundamentally, bent-crystal microscopes can provide high spatial resolution over a cm-size field of view, and typically operate within a narrow spectral bandwidth ($\lambda/\Delta\lambda \sim 10^{-3}$-$10^{-4}$), which results in nearly monochromatic images ([28], [29]).

2.1. Instrument design

X-ray diffraction from a crystalline solid is the coherent reflection of x-rays from the crystal's lattice in which the x-ray's wavelength and the crystal's *d*-spacing satisfy Bragg's Law. A polycrystalline sample consists of a large number of randomly oriented individual crystals, thus a large number of them with the correct orientation will satisfy Bragg's Law [30]. When a polycrystalline sample is illuminated by a monochromatic x-ray beam, the x-rays are diffracted into scattering patterns called Debye-Scherrer cones, as shown in Figure 2-1. By fielding a 2D x-ray detector that intersects a plane of multiple diffraction cones, a polycrystalline or powder XRD pattern may be obtained.

As shown in the previous section, any x-ray detector that stores the data locally, placed near the Z-DMP load would be destroyed before the powder XRD pattern could be recovered. To circumvent this issue, a spherically bent crystal (otherwise denoted as a "spherical crystal") is fielded in place of the x-ray detector to intersect the Debye-Scherrer cones and to relay-image the information to a detector that is well-protected from the debris field.

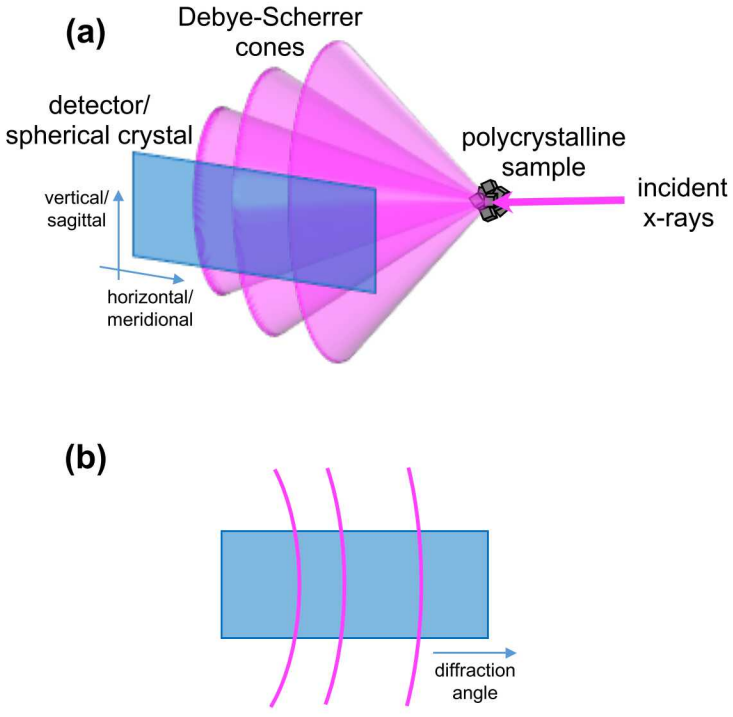

Figure 2-1. (a) Illustration of powder x-ray diffraction from a polycrystalline sample. (b) Intersections of portions of Debye-Scherrer cones with a 2D x-ray detector/spherical crystal.

Figure 2-2 shows how the bent-crystal imaging concept is utilized to measure x-rays that are diffracted from a Z-DMP load sample. First, the Z-Beamlet (ZBL) laser is focused onto an x-ray target to generate incident x-rays to an XRD sample on the Z-DMP load. Then, the diffracted x-rays are reflected off the surface of a spherical crystal with a radius of curvature R. A key aspect of the scheme is that the XRD sample is located on the Rowland circle (with a diameter R), which is the locus of focal points such that points on the circle are focused back onto the circle. Since bent-crystal x-ray imaging relies on Bragg diffraction of x-rays from its crystal planes, only x-rays with wavelength,

$$\lambda = \frac{2d}{n} \sin \theta_B, \qquad (1)$$

or corresponding photon energy,

$$\boldsymbol{E = \frac{nhc}{2d \sin \theta_B}}, \qquad (2)$$

that satisfy the Bragg condition are reflected by the crystal lattice. In Equations (1) and (2), n is the reflection order (an integer ≥ 1), hc is the Planck constant times the speed of light, d is the spacing of the crystal lattice planes, θ_B is the Bragg angle between the incident ray and the crystal plane. Spherical crystal imaging systems usually operate near-normal angle of incidence ($\theta_B \approx$ 80-90°) in order to reduce aberrations and optimize image resolution. However, to accommodate the unique geometry of XRD, the SCDI scheme operates at lower angles of incidence ($\theta_B \approx$ 60-70°) while maintaining acceptable imaging quality.

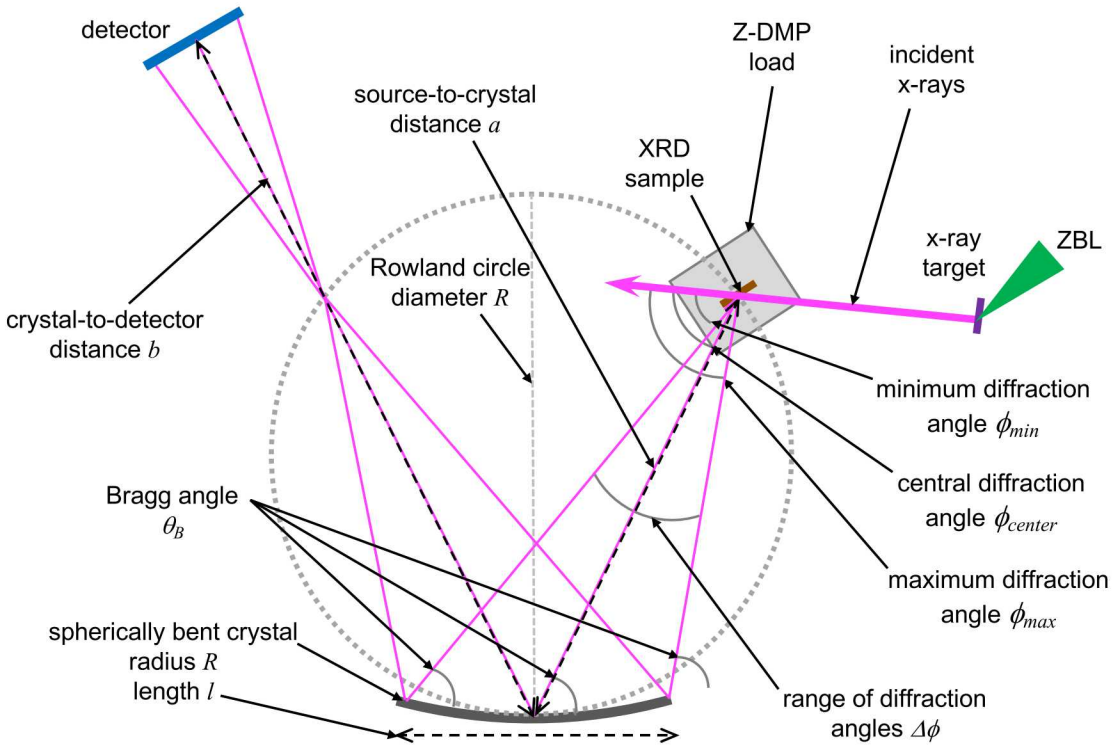

Figure 2-2. Operational schematic of the SCDI diagnostic viewed in the meridional (horizontal) plane.

The measured range of diffraction angles $\Delta\phi$ is determined by the spherical crystal's length l, while the minimum and maximum diffraction angles, ϕ_{min} and ϕ_{max}, may be varied by adjusting the x-ray target's incident angle relative to the XRD sample. The source-to-crystal distance a is measured from the XRD sample to the spherical crystal's center along the ray of the central diffraction angle ϕ_{center}, and connects to the center of the detector with the crystal-to-detector distance b. The x-ray reflection in this focusing geometry is described by the spherical lens equation,

$$\frac{1}{a}+\frac{1}{b}=\frac{1}{f}, \qquad (3)$$

where the focal lengths in the sagittal (vertical) and meridional (horizontal) planes are given as,

$$f_{sag}=\frac{R}{2\sin\theta_B}, \qquad (4)$$

and

$$f_{mer}=\frac{R\sin\theta_B}{2}, \qquad (5)$$

respectively. The location of the x-ray detector is chosen such that the image is focused in the sagittal (vertical) direction while maintaining sufficient angular spread within the meridional plane. Thus, the crystal-to-detector distance b is obtained from Equations (3) and (4).

Bent-crystal microscopes have typically utilized various single-crystals (e.g., quartz, mica, silicon or germanium [31]) to achieve imaging with high spatial resolution ($\Delta x \approx 10$ μm). Although highly oriented pyrolytic graphite (HOPG) crystals due to their intrinsic mosaic spread, have much lower spatial resolution, they have about 10-100 × higher x-ray collection efficiency than quartz, mica, and germanium crystals [32]. Because of the inherently low signal levels of XRD, a spherically bent HOPG crystal was chosen for the SCDI diagnostic to maximize x-ray throughput.

To generate x-rays for XRD on Z, the ZBL beam is focused onto a metal foil target, forming a high temperature plasma that emits K-shell line radiation [33]. The He-like emissions, specifically He_α lines, of various metals with a range of x-ray photon energies (4-10 keV) are listed in Table 2-1, along with their corresponding possible SCDI configuration for a spherical HOPG crystal with a chosen 150 mm radius of curvature. The spherical crystal's radius of curvature was selected based the following criteria. First, a spherical crystal with a small radius can be located close to the XRD sample, thus maximizing the solid angle of diffracted x-rays collected. However, if the radius becomes too small then spherical aberrations are noticeably prominent. In addition, the spherical crystal's radius has to be large enough so the detector housing does not interfere with the Z-DMP load hardware.

The x-ray target's photon energy/wavelength determines its *1/e* attenuation depth into the spherical HOPG crystal, the order of reflection, and the Bragg angle. Generally, a spherical crystal's reflection efficiency decreases at higher orders of reflections. Selecting the appropriate x-ray target depends on the specific sample to be investigated by XRD, but usually higher atomic number materials require higher photon energies. By leveraging the successful implementation of the ZBL x-ray backlighter diagnostic on Z, the initial SCDI diagnostic is designed around a Mn x-ray target's He_α (6.181 keV) emission. This enables XRD measurements of various low-Z materials (e.g., beryllium, boron, carbon compounds), where the x-rays can penetrate sufficiently deep into the sample.

Table 2-1. Possible SCDI configurations using He_α x-rays and the spherical HOPG crystal ($2d$ = 6.708 Å, r = 150 mm).

X-ray Source He_α	Photon Energy (keV)	Wavelength (Å)	Attenuation Length $x_{1/e}$ (mm)	Reflection Order n	Lattice Spacing $2d/n$ (Å)	Bragg Angle θ_B (°)	Source-to-Crystal Distance a (mm)	Crystal-to-Detector Distance b (mm)
Ti	4.750	2.611	0.205	2	3.354	51.1	117	552
V	5.205	2.382	0.270	2	3.354	45.3	107	1179
Cr	5.682	2.182	0.355	3	2.236	77.4	146	162
Mn	**6.181**	**2.006**	**0.465**	**3**	**2.236**	**63.8**	**135**	**221**
Fe	6.701	1.851	0.595	3	2.236	55.9	124	336
Co	7.242	1.712	0.760	3	2.236	50.0	115	665
Ni	7.806	1.589	0.960	4	1.677	71.3	142	179
Cu	8.392	1.478	1.200	4	1.677	61.8	132	239
Zn	8.999	1.378	1.495	4	1.677	55.3	123	352
Ga	9.628	1.288	1.840	4	1.677	50.2	115	641

2.2. Hardware Implementation

The SCDI diagnostic consists of two main hardware components: (1) an imager ring, and (2) a detector housing, as shown in Figure 2-3. The imager ring (~30 cm diameter) encompasses the Z-DMP load, and enables all of the other SCDI parts to be mounted directly on it. The ZBL x-ray target is mounted on the imager ring at a distance of 4" (101.6 mm) from the XRD sample on the Z-DMP load. The spherical HOPG crystal is attached to a tip/tilt base and mounted on the imager ring at a distance of 135 mm from the XRD sample. The spherical HOPG crystal is vertically 30 mm tall and horizontally 75 mm long, which at the source-to-crystal distance of 135 mm enables collections of XRD patterns over a range of diffraction angles of about $\Delta\phi \approx 30°$. A cross-over aperture block with a rectangular opening (3 mm wide x 15 mm tall) is mounted on the imager ring such that it is centered on the Rowland circle.

To align the SCDI diagnostic, a laser diode is initially fielded at the x-ray target location. The laser beam passes through an input collimator and is centered on the XRD sample. The laser beam is reflected off the XRD sample and onto the spherical HOPG crystal. By adjusting the spherical HOPG crystal's tip/tilt, the laser beam is focused and directed through the cross-over aperture and into the detector housing. The laser diode is then replaced by the x-ray target.

The detector housing is wedge-shaped with interior dimensions of about 150 mm long x 100 mm wide x 75 mm tall. It is made of 1-inch thick tungsten walls to shield against the x-ray background coming from Z during the experiment. For load debris protection, an outer layer of sacrificial material (e.g., aluminum/steel) is attached to the side of the housing closest to the Z-DMP load. Inside the detector housing, a Fuji MS-type image plate (IP) detector is used to record the diffracted x-rays. The image plate detector was chosen for multiple reasons. First, it is a reusable and robust recording medium consisting of highly x-ray sensitive material made from $BaF(Br,I):Eu^{2+}$ phosphor crystals suspended in a plastic binder [34]. Second, IP is capable of detecting x-rays with 1–100 keV photon energies, and has a dynamic range much larger than x-ray film ([35], [36], [37]). Finally, IP is immune

to the electromagnetic pulse interference arising from the Z-accelerator. The IP is 75 mm wide by 35 mm tall, and is contained inside a cassette that is retrieved after the Z-XRD experiment.

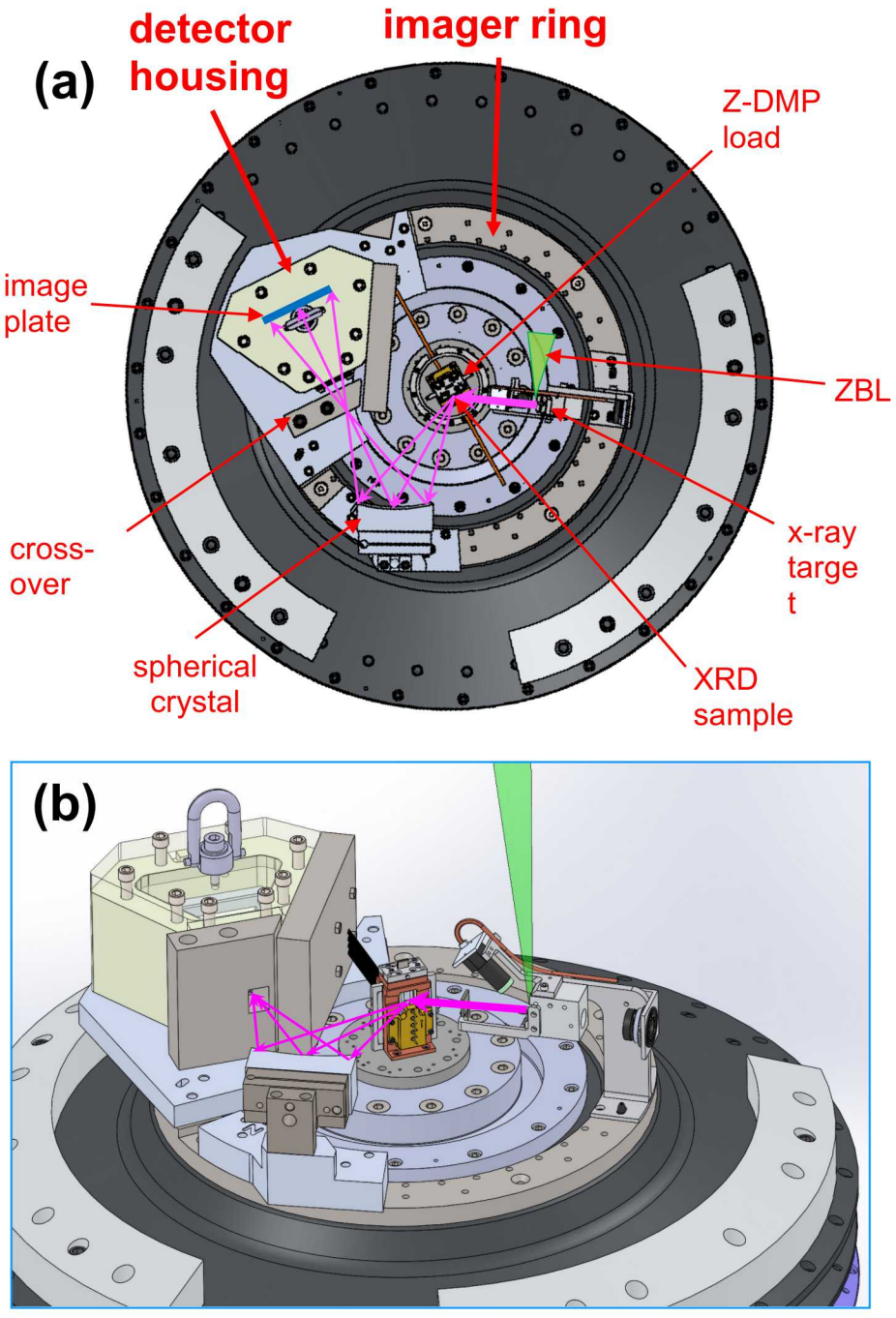

Figure 2-3. Spherical crystal diffraction imager (SCDI) diagnostic on a Z-DMP experiment: (a) top view, and (b) isometric view.

2.3. Calibration of SCDI diagnostic

We performed experiments using a surrogate Z-DMP load setup in the Z-Backlighter Facility's Chama target chamber to calibrate the SCDI diagnostic, as shown in Figure 2-4. Beryllium (Be) was chosen as the Z-XRD sample for several reasons. First, for 6.2 keV x-rays, Be has a high coherent scattering cross-section of 0.12 cm^2/g [38], and a hexagonal close packed (hcp) structure that produces a sufficiently strong XRD pattern. Second, Be has a substantial *1/e* attenuation depth of 2.5 mm for the 6.2 keV x-rays, which enables the Be sample to serve as its own, x-ray transparent, window during shock-loading on Z. Hence, the XRD measurement will consist of shocked and un-shocked Be, and there is no need to contend with extraneous diffraction from a window material of different chemistry.

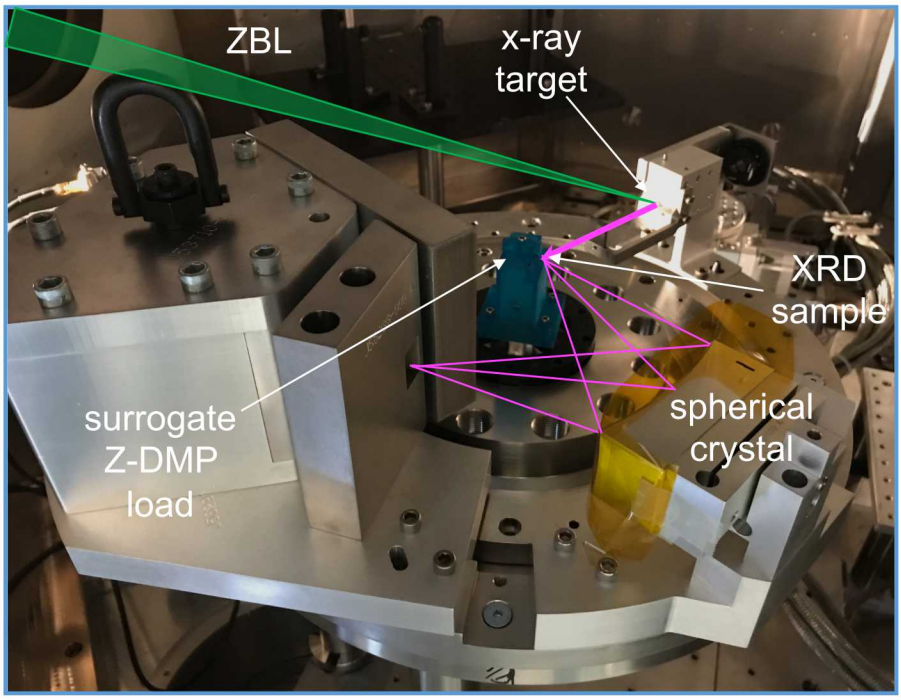

Figure 2-4. SCDI setup in the Chama target chamber.

In the Chama chamber, an ambient Be sample (1.5 mm thick × 5 mm wide × 7.5 mm tall) was mounted on a 3D-printed surrogate Z-DMP load. The ZBL beam was focused onto a Mn x-ray target to generate He_α x-rays with photon energy of 6.181 keV. The measured XRD pattern (shot B18122000) at the spherical crystal location is shown in Figure 2-5. For a quantitative analysis of the XRD pattern, the 2D image needs to be integrated spatially to generate an intensity vs. diffraction angle plot.

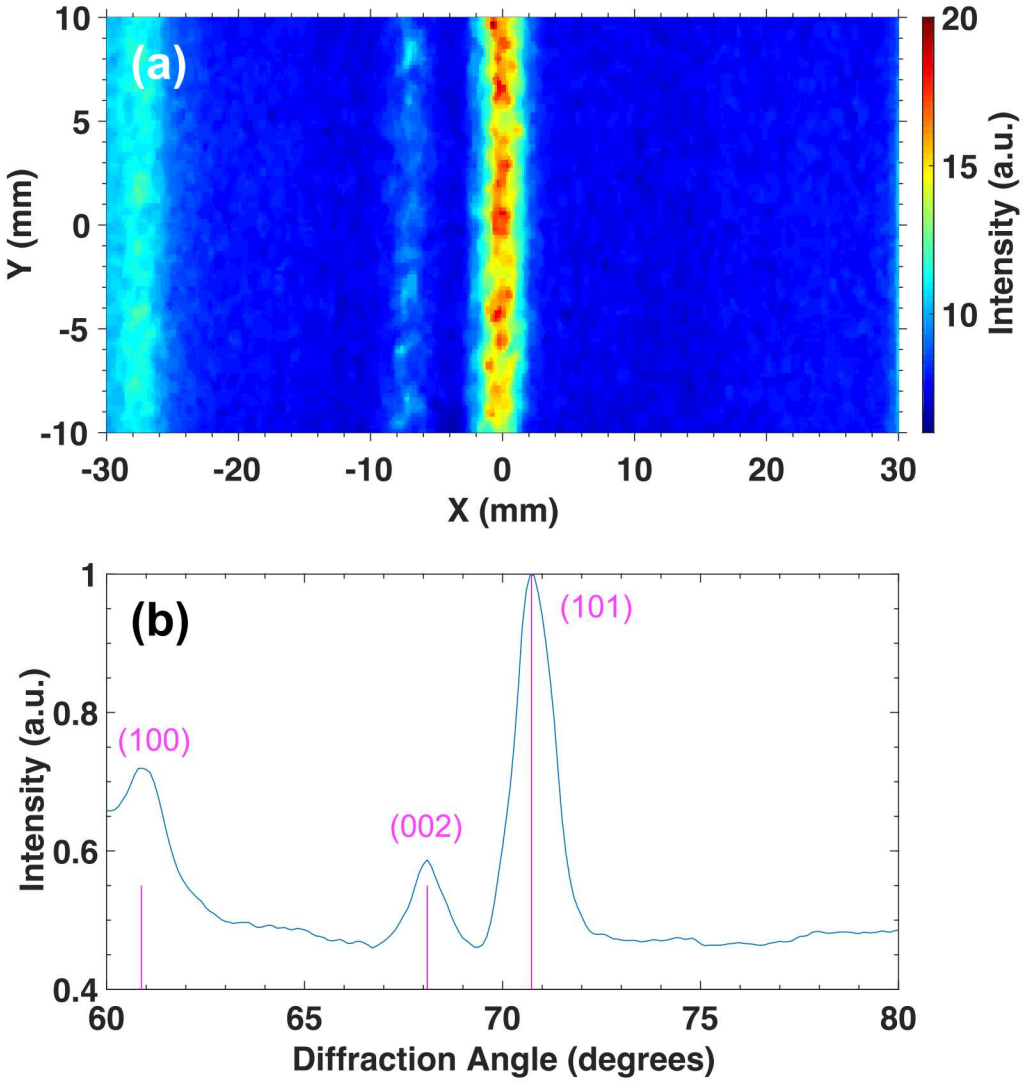

Figure 2-5. ZBL shot B18122000: Direct XRD at the SCDI's spherical crystal location, (a) measured XRD image, and (b) integrated line profile vs diffraction angle. Miller indices are marked with vertical lines.

A new analysis code was written using Matlab to integrate the measured XRD pattern, and is included as a "Diffraction Class" in the Sandia Matlab AnalysiS Hierarchy (SMASH) toolbox [39]. The analysis of the XRD pattern starts by mapping the image using the appropriate experimental parameters. The image's vertical axis represents the spatial extent of the XRD pattern, while the horizontal axis is converted to the corresponding diffraction angles. Then, the image is integrated along arcs corresponding to the intersection of the Debye-Scherrer cones with the x-ray detector for each diffraction angle.

The ambient Be sample's hcp structure is used to calibrate the analysis parameters, which identify the 3 diffraction peaks, at 60.9°, 68.1°, and 70.7° from the (100), (002), and (101) *hkl* planes, respectively. The full-width-at-half-maximum (FWHM) widths of the diffraction peaks were measured to be about 0.5°, which is mainly due to volume broadening by the scattering throughout the Be sample's 1.5 mm thickness. The 2 closest diffraction peaks at 68.1° and 70.7° are clearly resolved.

The spherical HOPG crystal was manufactured by diamond-machining an aluminum substrate to radius of curvature of 150 mm [40], and then coating a 0.3 mm thick layer of HOPG onto the spherical surface [41]. The Mn x-ray target was positioned so the central diffraction angle incident to the spherical HOPG crystal was at 70° with respect to the surface. The measured XRD pattern (shot B18110903) inside the SCDI housing is shown in Figure 2-6. The range of diffraction angles covered by the SCDI is from 55° to 85°, thus all 3 diffraction peaks of the Be-hcp sample are clearly detected. As expected, the peaks are vertically compressed due to the sagittal focusing. Meanwhile, the angular resolution of the diffraction peaks is reduced to a FWHM of about 1.5° due to the mosaic spread of the HOPG.

Next, the Mn x-ray target was re-positioned so the central diffraction angle incident to the spherical HOPG crystal was at 80° (shifted by 10°). The measured XRD pattern (shot B19013104) inside the SCDI housing is shown in Figure 2-7. Since the new range of diffraction angles covered by the SCDI is from 65° to 95°, only the 2 diffraction peaks of the Be-hcp sample at 68.1° and 70.7° are measured. This configuration has the advantage of having an open region at higher diffraction angles where the shifted diffraction peaks of the compressed material are expected.

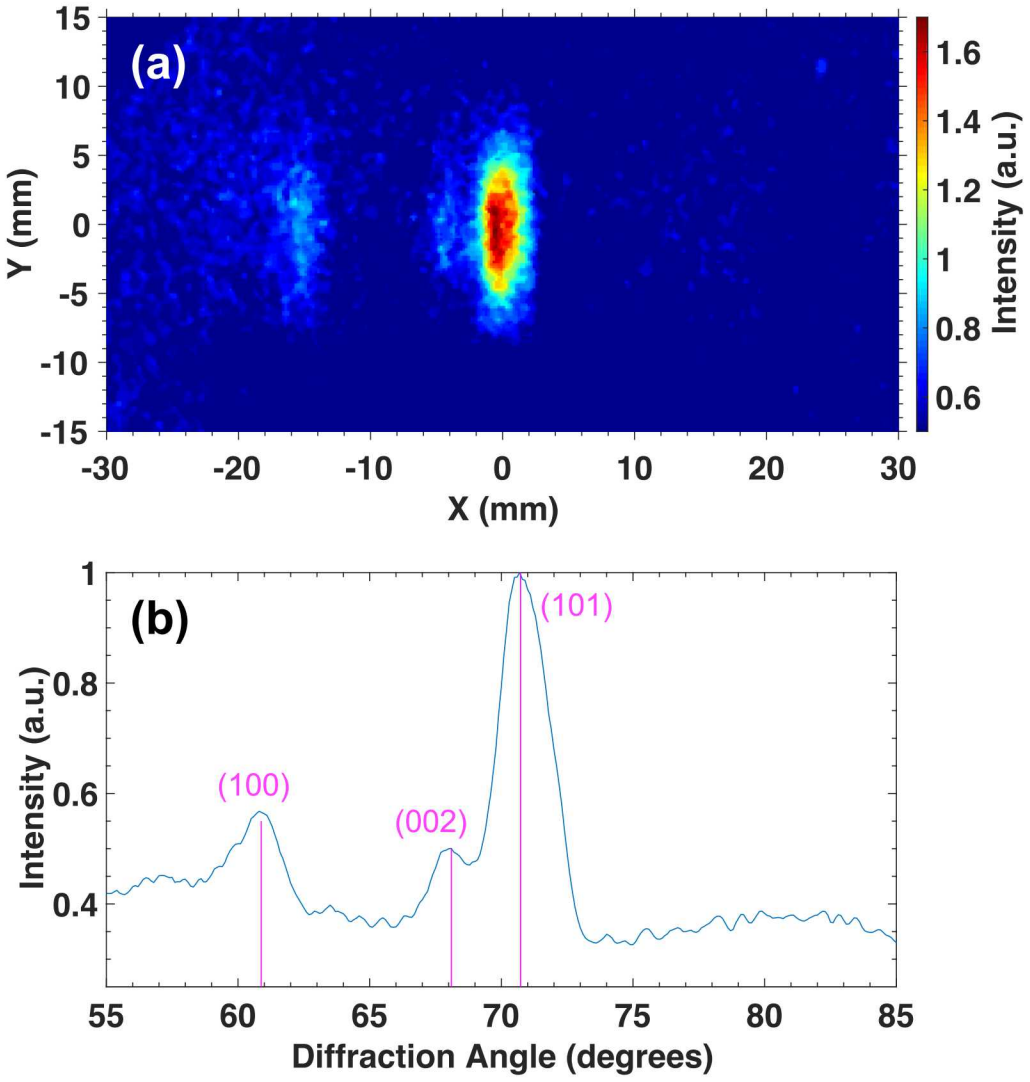

Figure 2-6. ZBL shot B18110903: SCDI central diffraction angle at 70°, (a) measured XRD image, and (b) integrated line profile vs diffraction angle. Miller indices are marked with vertical lines.

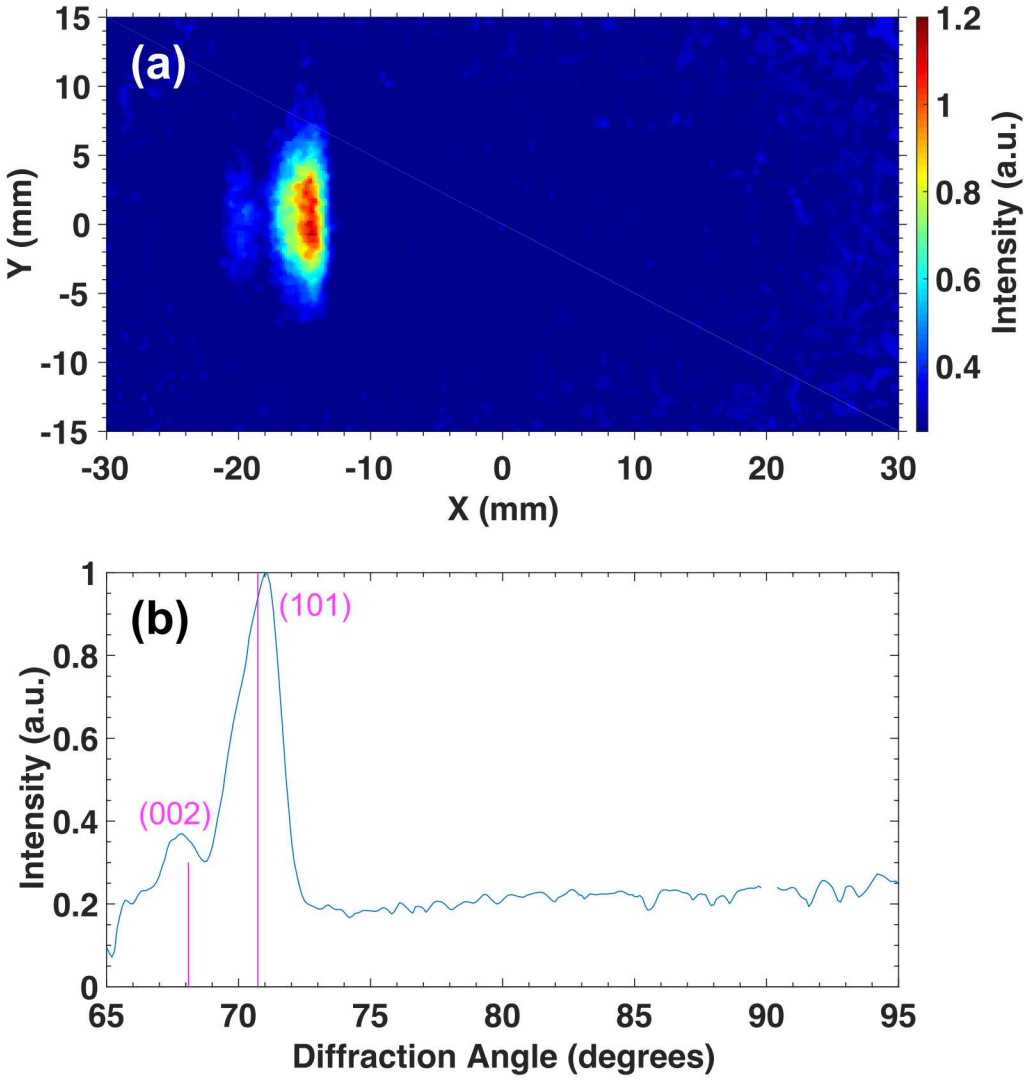

Figure 2-7. ZBL shot B19013104: SCDI central diffraction angle at 80°, (a) measured XRD image, and (b) integrated line profile vs diffraction angle. Miller indices are marked with vertical lines.

3. X-RAY DIFFRACTION EXPERIMENTS ON Z

We preformed 4 Z-DMP experiments (Z3325, Z3362, Z3391, and Z3396) implement XRD on the Z Pulsed Power Facility in FY2019. The corresponding experimental parameters for these Z-XRD experiments are listed in Table 3-1. All 4 Z-XRD experiments used a Z-DMP coaxial load that consisted of a symmetric 9 mm wide x 2 mm thick tungsten cathode stalk with 1.2 mm thick anode Al flyer plates. Figure 3-1 shows the images of the north and south panels of the Z-DMP load assembly.

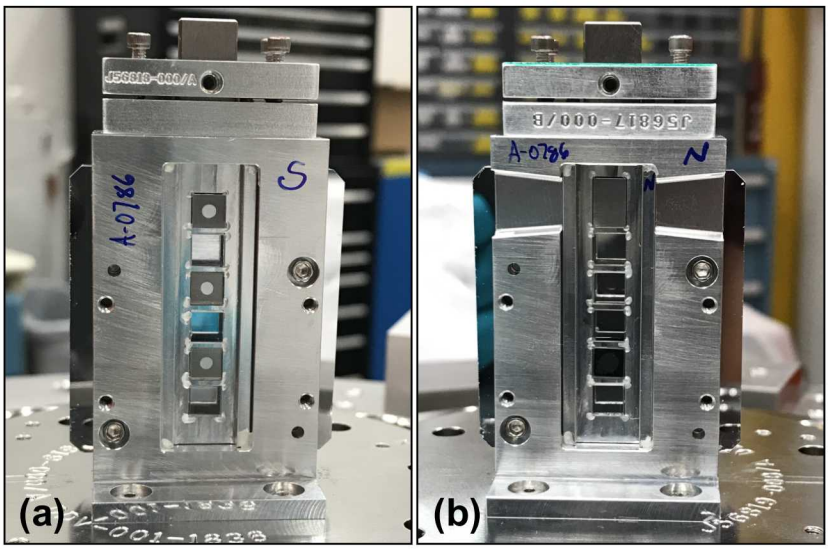

Figure 3-1. Images of the Z-DMP load assembly (a) south, and (b) north panels.

Figure 3-2 shows the pre-shot and post-shot images of the Z-XRD experimental setup in the Z Center Section. During the Z-XRD experiment, the Z-DMP load, ZBL x-ray target, and spherical HOPG crystal were completely destroyed. However, the IP was protected within the SCDI detector housing and was able to be retrieved afterwards.

Table 3-1. Z-XRD experimental setup parameters.

Z Shot Number	Z Hardware Number	Marx Charge Voltage (kV)	Be Sample Thickness (mm)	SCDI Central Diffraction Angle ϕ_{center}(°)	SCDI Diffraction Range $\Delta\phi$(°)
Z3325	A0786A	50	1.5	70	55-85
Z3362	A0771A	50	1.5	80	65-95
Z3391	A0856A	54	1.0	80	65-95
Z3396	A0865A	50	1.0	80	65-95

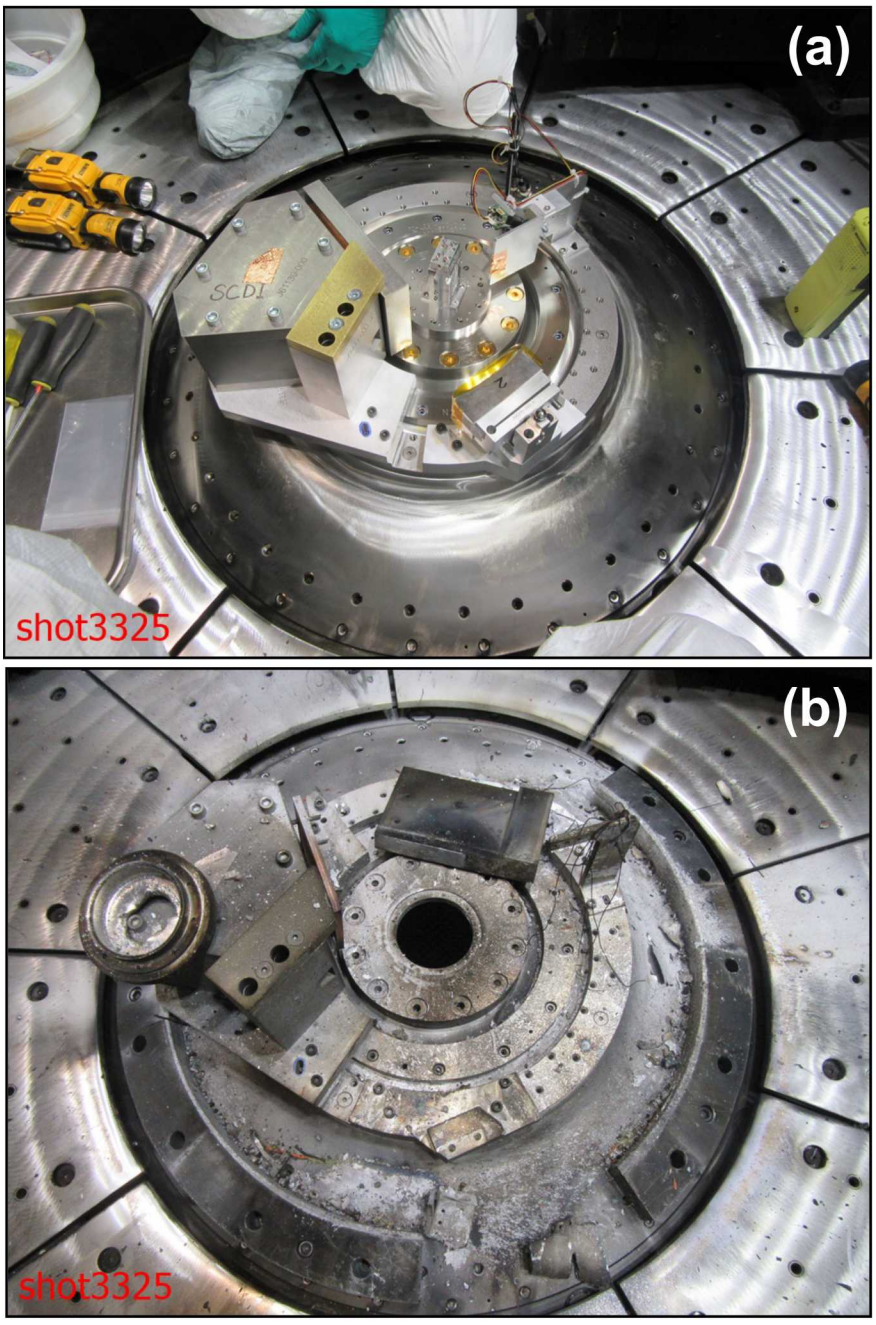

Figure 3-2. Images of the (a) pre-shot and (b) post-shot of the Z-XRD experiment.

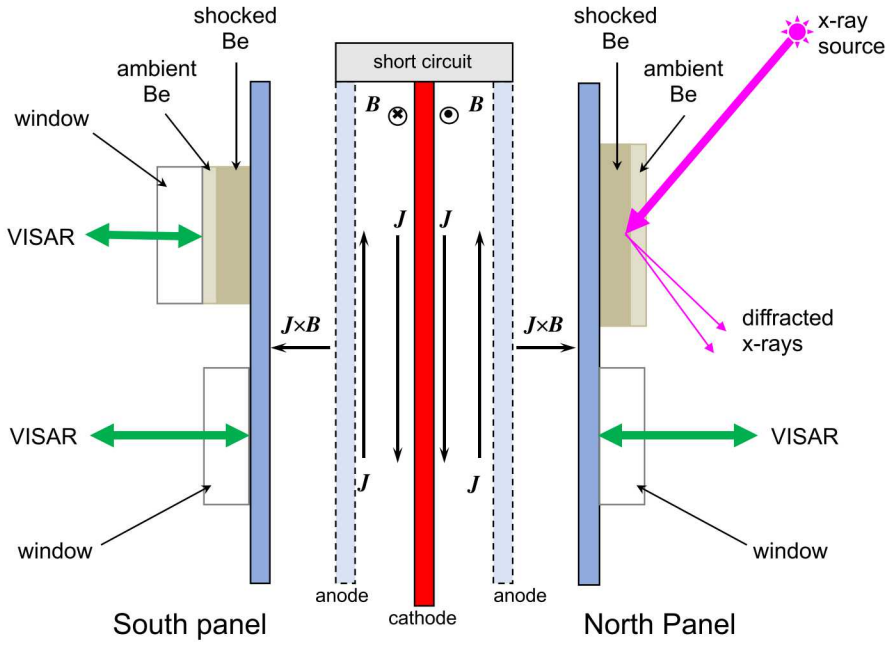

Figure 3-3. Cross-section view of the Z-DMP load with the Be samples probed by XRD and VISAR.

Figure 3-3 shows the locations of the samples used for the experiments. On the north panel's top position, a Be sample (5 mm wide x 7.5 mm tall) was probed by x-rays for XRD. At the opposite location on the south panel, a Be sample (5 mm wide x 5 mm tall) with the same thickness was backed by a window and probed by VISAR to obtain velocimetry data. Specifically, VISAR measured the shock arrival time ($t_{breakout}$) at the Be/window interface, which was used to obtain the shock velocity within the Be sample and its corresponding high-pressure state from the SESAME EOS Table 2010 for Be [42] . Windows below the Be samples were probed by VISAR to obtain the anode flyer plate velocity (v_{impact}) and impact time (t_{impact}), which combined with the ZBL arrival time (t_{ZBL}) determined the amount of shocked Be probed by the x-rays and measured by the SCDI diagnostic. The VISAR and SCDI results are presented in the following section, and summarized in Table 3-2.

Table 3-2. Z-XRD measurements from VISAR and SCDI diagnostics.

Z Shot Number	Flyer Impact Velocity v_{impact} (km/s)	ZBL Total Energy (J)	Flyer Impact Time t_{impact} (ns)	ZBL Arrival Time t_{ZBL} (ns)	Be Shock Breakout Time $t_{breakout}$ (ns)	Be Shock Pressure (GPa)
Z3325	12.7	2621	3379	3429	3474	202
Z3362	11.9	2204	3462	3490	3559	182
Z3391	13.5	2302	3372	3405	3435	223
Z3396	11.7	-	3420	-	3486	178

3.1. Results

3.1.1. Z3325

Z3325 went downline with a 50-kV shaped pulse and the hardware set A0786A, which had 1.5 mm thick Be samples. Figure 3-4(a) shows that the measured flyer impact velocity of v_{impact} = 12.7 km/s occurred at t_{impact} = 3379 ns. The shock propagated all the way through the 1.5 mm thick Be sample at $t_{breakout}$ = 3474 ns (95 ns transit time). The ZBL beam was fired into Z and onto a Mn x-ray target at t_{ZBL} = 3429 ns, which consisted of a pre-pulse (181 J, 0.5 ns) and a main pulse (2440 J, 3 ns). ZBL was timed 50 ns after impact to generate x-rays after the shock front had propagated ~ 1 mm into the Be, thus probing ~ 0.5 mm of shocked state (202 GPa) and a remaining ~ 0.5 mm of ambient state.

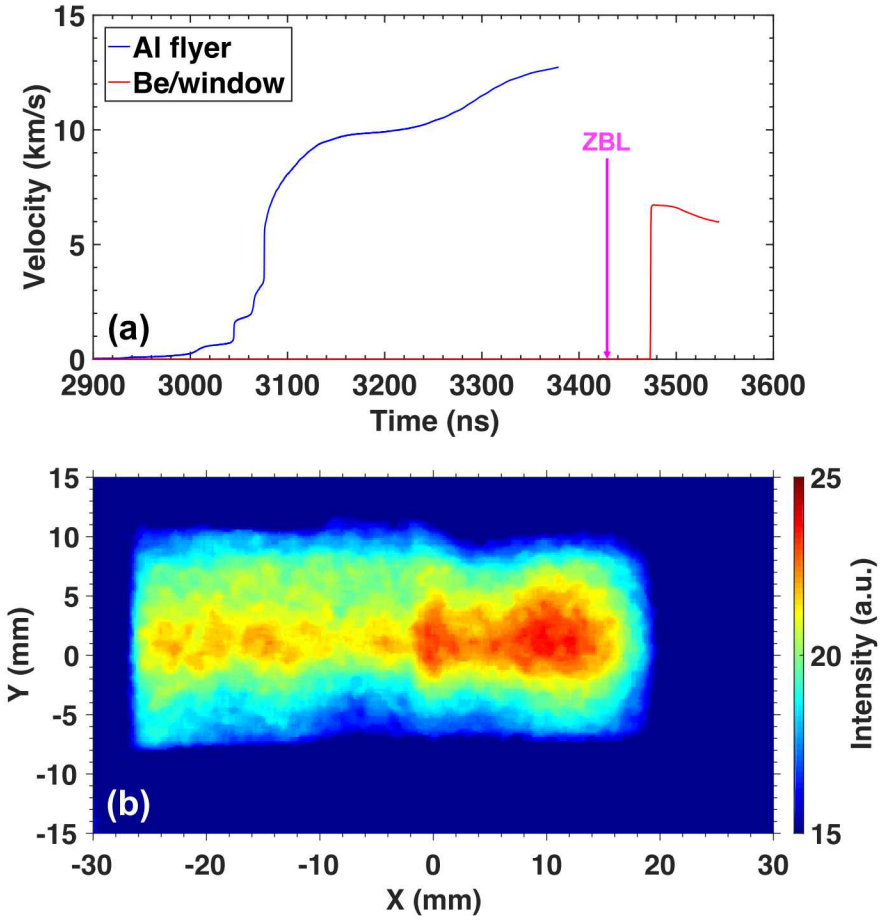

Figure 3-4. Z3325: (a) VISAR velocimetry data, and (b) SCDI x-ray diffraction data.

The Mn x-ray target was positioned so the central diffraction angle incident to the spherical HOPG crystal was at 70°. The measured XRD data by the SCDI diagnostic is shown in Figure 3-4(b). A widespread x-ray background was measured on the SCDI IP due to the tremendous amount of energy released when Z fires. Nonetheless, the 3 XRD peaks from the ambient Be material were indeed observed on the left side of the IP, as expected from the pre-shot calibration measurement (see Figure 2-6). However, the XRD signal from the shocked-compressed Be material, predicted to be on the right side of the IP, was obscured by a localized x-ray background feature. This unwanted

feature was hypothesized to be direct emission from the Z-DMP load that was reflected by the spherical HOPG crystal onto the SCDI IP. Further investigation of this issue is presented later in this section.

3.1.2. Z3362

Z3362 went downline with a 50-kV shaped pulse and the hardware set A0771A, which had 1.5 mm thick Be samples. (a) shows v_{impact} = 11.9 km/s, t_{impact} = 3462 ns, and $t_{breakout}$ = 3559 ns. The ZBL timing was t_{ZBL} = 3490 ns, which consisted of a 132 J pre-pulse and a 2072 J main pulse. This corresponded to ZBL was timed at 28 ns after impact, which generated the x-rays after the shock front had propagated ~ 0.5 mm into the Be, thus probing a ~ 0.3 mm thick shocked state (182 GPa) and a remaining ~ 1.0 mm thick of ambient state.

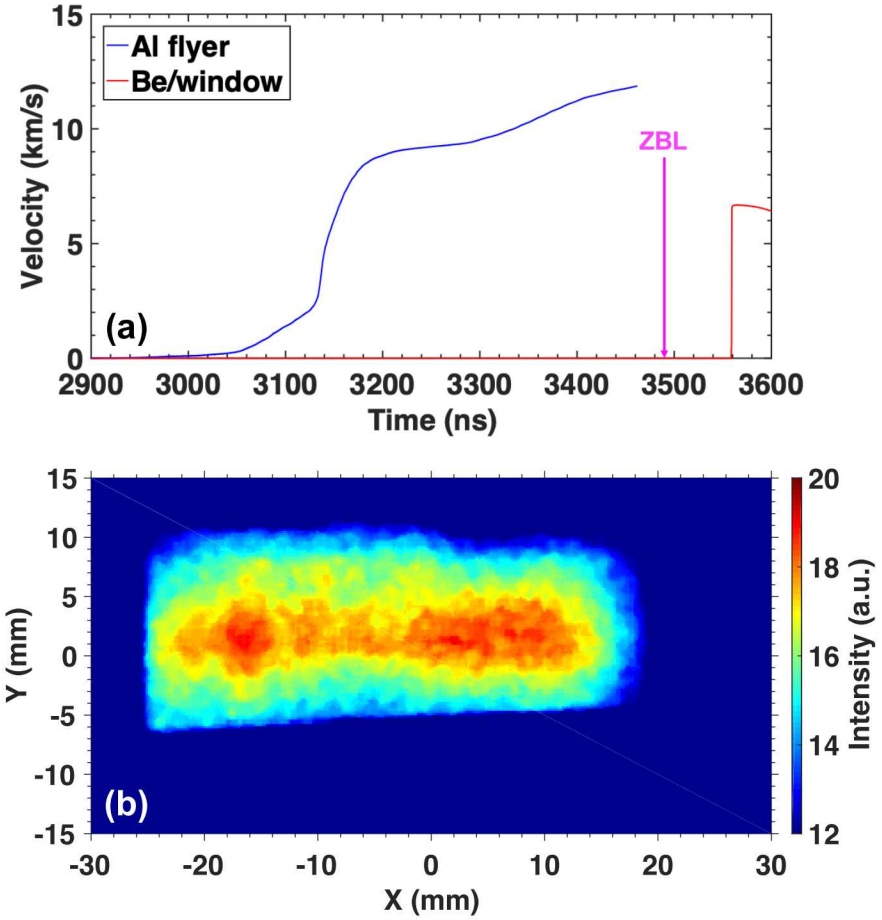

Figure 3-5. Z3362: (a) VISAR velocimetry data, and (b) SCDI x-ray diffraction data.

In order to allow more of the compressed diffraction lines to be observed, the Mn x-ray target was positioned so the central diffraction angle incident to the spherical HOPG crystal was at 80°. The measured XRD data by the SCDI diagnostic is shown in Figure 3-5(b). Although the x-ray background remains higher than desired, additional tungsten shielding within the SCDI housing was able to cut the x-ray background in half (compared to Z3325). The 2 XRD peaks from the ambient Be material were observed on the IP's far-left side, which compared well with the pre-shot calibration (see Figure

2-7). Once again, the x-ray background from the Z-DMP load obscured the shocked Be XRD signal on the IP's right side.

3.1.3. Z3391

Z3391 went downline with a 54-kV shaped pulse and the hardware set A0856A, which had 1.0 mm thick Be samples. Figure 3-6(a) shows v_{impact} = 13.5 km/s, t_{impact} = 3372 ns, and $t_{breakout}$ = 3435 ns. The ZBL timing was t_{ZBL} = 3405 ns, consisting of a 135 J pre-pulse and a 2167 J main pulse. ZBL was timed at 33 ns after impact to generate x-rays after the shock front had propagated ~ 0.6 mm into the Be, thus probing a ~ 0.3 mm thick shocked state (223 GPa) and a remaining ~ 0.4 mm thick ambient state.

Using the SCDI setup with central diffraction angle at 80°, the measured XRD data is shown in Figure 3-6(b). For this Z-XRD experiment, a hole (8 mm diameter) was cut into the top left portion of the SCDI IP for an x-ray photodiode to measure the time-history of the x-ray background inside the SCDI housing. Unfortunately, the x-ray photodiode measured mainly noise from the EMP of Z firing.

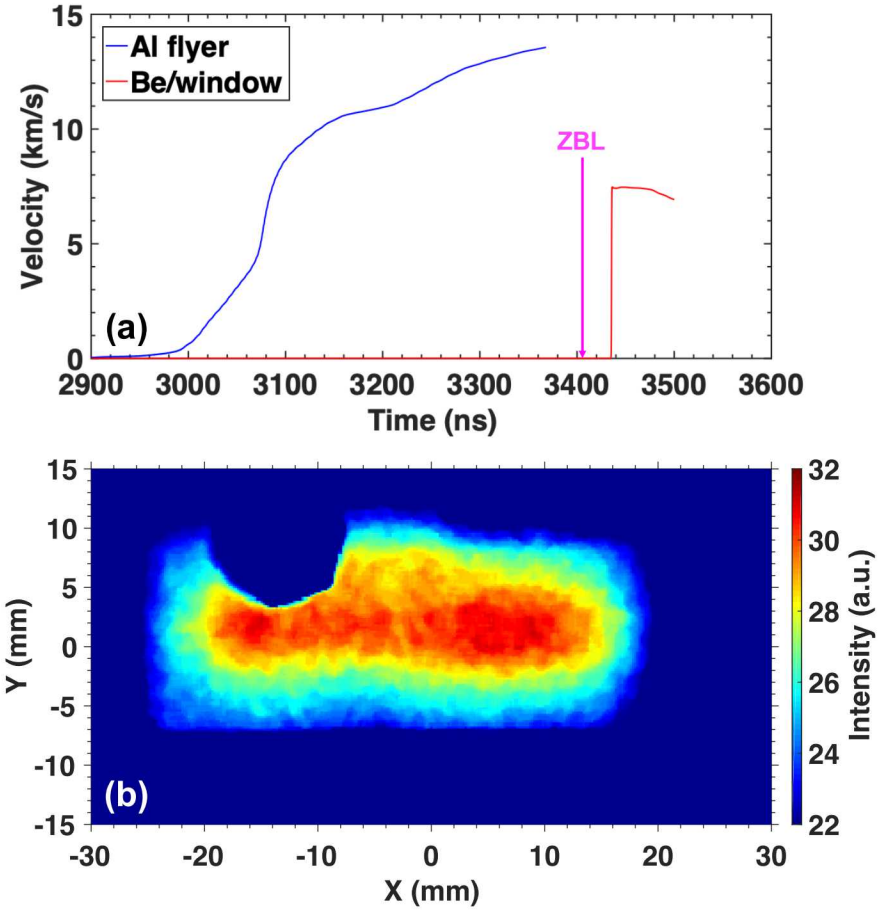

Figure 3-6. Z3391: (a) VISAR velocimetry data, and (b) SCDI x-ray diffraction data.

3.1.4. Z3396

Z3396 went downline with a 50-kV shaped pulse and the hardware set A0856A, which had 1.0 mm thick Be samples. Figure 3-7 shows v_{impact} = 11.7 km/s, t_{impact} = 3420 ns, and $t_{breakout}$ = 3486 ns. The shock pressure of 178 GPa was similar to that achieved on Z3362.

This was designed to be a "null" shot, so ZBL was not fired, thus no XRD was measured from the Be sample with the SCDI diagnostic. Instead, the SCDI measured directly the x-ray background feature from the Z-DMP load. The resultant image shows a bright emission feature on the right side, nearly identical in shape to the background observed on the similar shot Z3362. The current flowing in-between the aluminum anode plate and tungsten cathode stalk has been known to generate hot plasma within the A-K gap. Although the temperature of that plasma has not been directly measured, we speculate that it generates enough x-rays that propagate through the Al load assembly to be measured by the very sensitive SCDI diagnostic. This null data will be used to elucidate the SCDI data from the previous Z-XRD experiments.

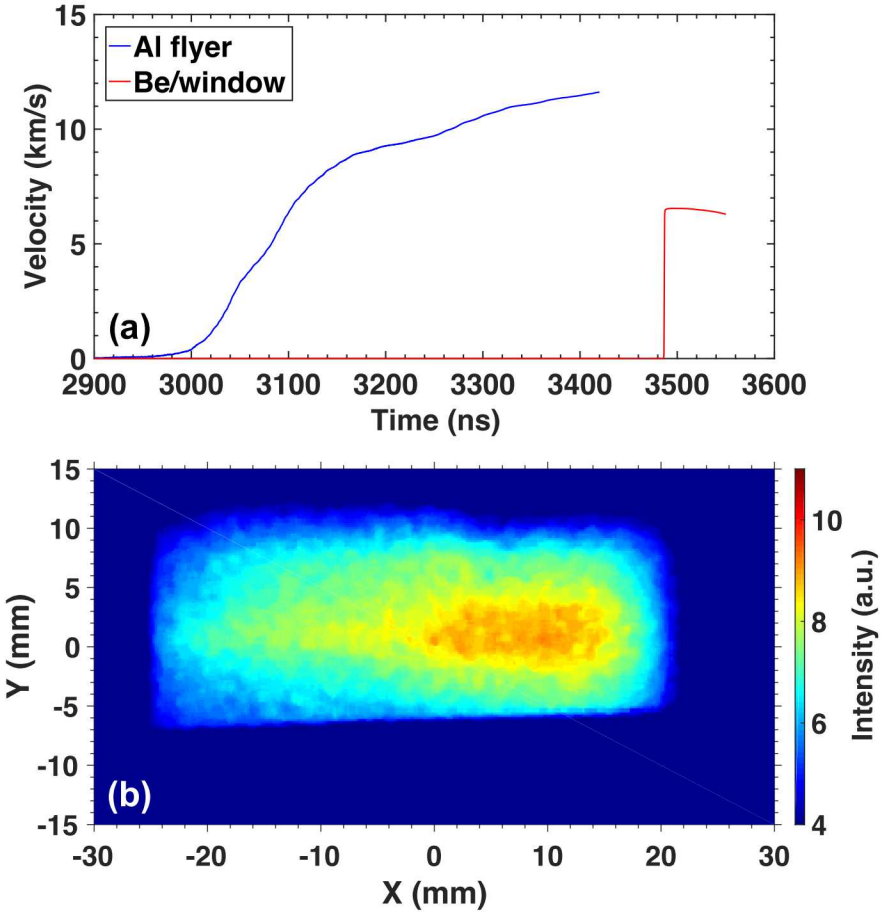

Figure 3-7. Z3396: (a) VISAR velocimetry data, and (b) SCDI x-ray diffraction data.

3.2. Analysis

3.2.1. Beryllium EOS and phase diagram

The EOS and phase diagram of Be has been of investigated both experimentally and theoretically because it has a wide range of applications in aircrafts, spacecrafts, communication satellites, nuclear power industry ([43], [44], [45], [46], [47]). At ambient pressure and temperature, Be is known be hexagonal close packed (hcp) with a nonideal *c/a* ratio. However, the rest of the phase diagram of Be is still quite poorly understood even at temperatures below melting and at pressures below 100 GPa. Recently, an *ab initio* three-phase EOS for elemental Be was constructed by Benedict *et al.* [48], which consisted of an ambient hcp solid phase, a high-temperature body centered cubic (bcc) solid phase, and a liquid phase (see Figure 3-8).

In early experiments by Francois and Contre [49], Be was heated at ambient pressure, and a solid-solid phase transition was reported, which was believed to be a bcc structure in a narrow range of temperature prior to melting. These experiments suggested that the hcp-bcc phase boundary has a negative slope, but subsequent work by Abey [50] suggests that it may be positive. However, recent diamond-anvil XRD measurements ([51], [52]) have been unable find evidence of the bcc phase of Be for temperature between 300 K and 4000 K, and pressures between 15 GPa and 205 GPa. To experimentally access the higher temperature and pressure states of Be, dynamic compression techniques are required, which provided additional motivation to use Be samples for the Z-XRD experiments. Specifically, the measured XRD data of shock-compressed Be on Z would benchmark the EOS and phase diagram of Be along a dynamic loading path.

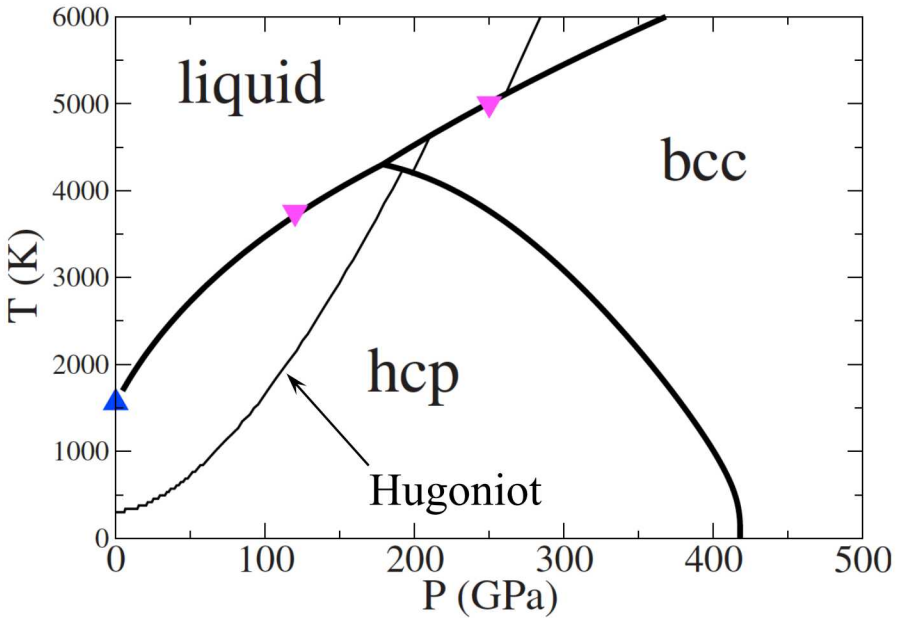

Figure 3-8. Phase diagram of Be from the EOS model described in Ref [48]. Upward triangle is the experimental ambient-pressure melt point, downward triangles are results from two-phase simulations melting from bcc. Thin lines denote the principal Hugoniot as computed by the EOS model.

3.2.2. *Integration of XRD pattern*

The SCDI data of the Z-XRD shots are analyzed using the Diffraction class of SMASH toolbox, as described in Section 2.3. Figure 3-9 shows the spatially integrated intensity vs diffraction angle plots from the SCDI diagnostic that measured XRD using the ZBL generated x-rays (Z3325, Z3362, and Z3391).

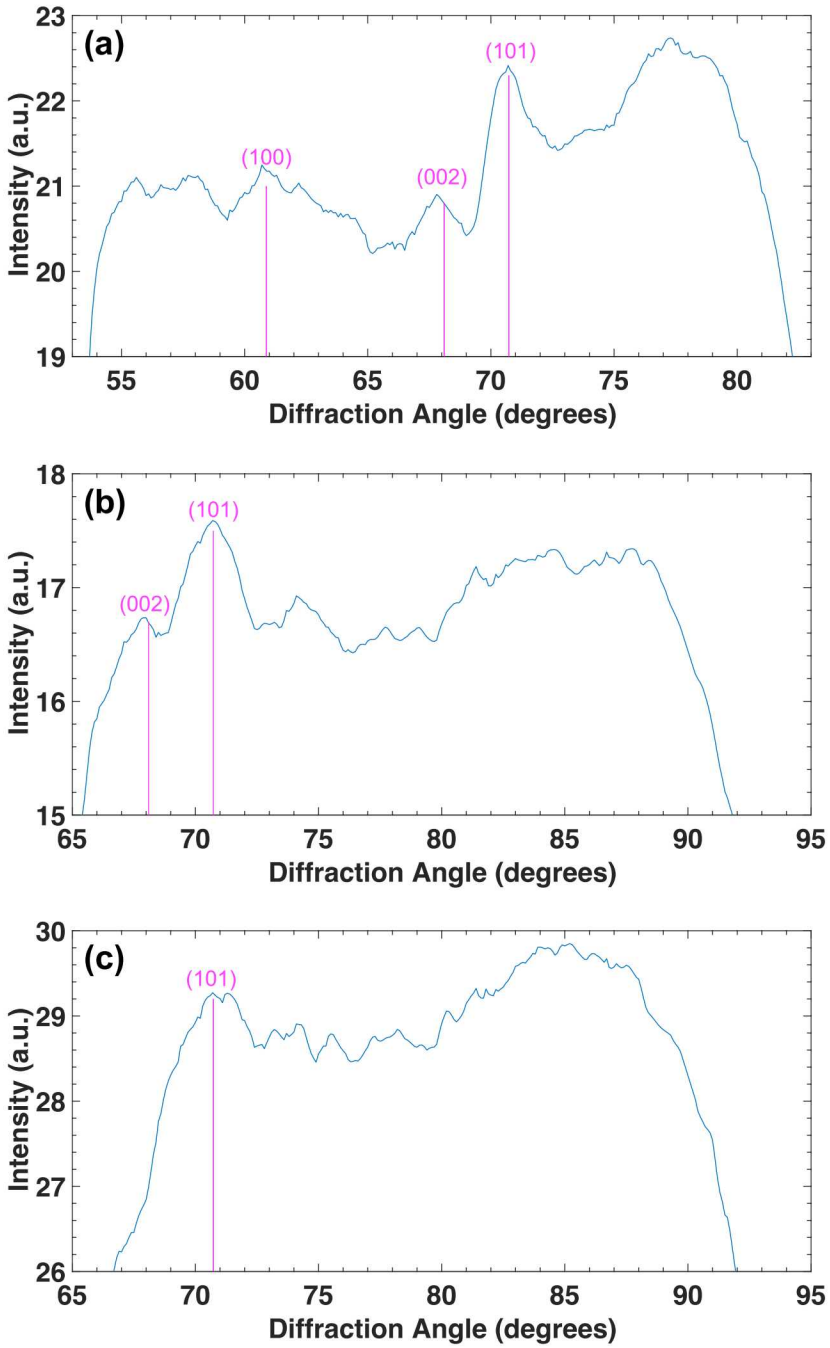

Figure 3-9. Integrated line profile vs diffraction angle for (a) Z3325, (b) Z3362, and (c) Z3391. Line profiles contain significant amount of unwanted background. Miller indices are marked with vertical lines.

For Z3325, with the SCDI diagnostic centered at the diffraction angle of ϕ_{center} = 70°, three XRD peaks from the unshocked Be are indexed in Figure 3-9(a). For Z3362, with the SCDI diagnostic centered at ϕ_{center} = 80°, two XRD peaks from the unshocked Be are indexed in Figure 3-9(b). Although the SCDI diagnostic was also centered at ϕ_{center} = 80° on Z3391, only one XRD peak from the unshocked Be is clearly indexed in Figure 3-9(c).

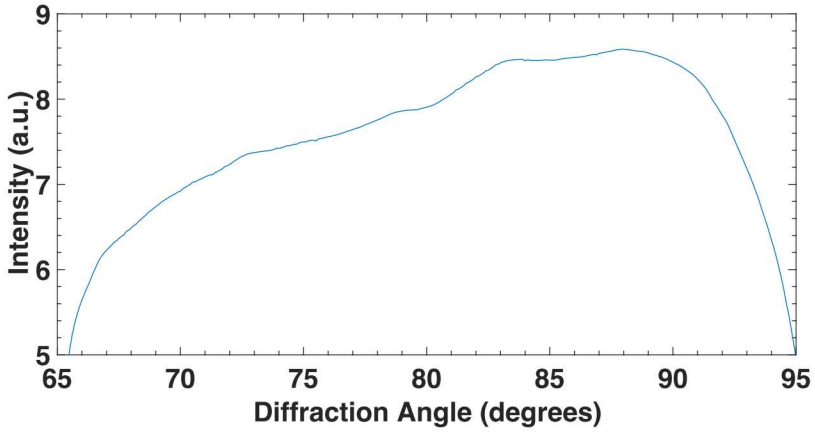

Figure 3-10. Integrated line profile vs diffraction angle illustrating the unwanted background recorded in Z3396.

For all of these Z-XRD experiments, the indexing of XRD peaks from shocked Be is hindered by unwanted background. Thus, to properly analyze the XRD data measured by the SCDI diagnostic, the unwanted x-ray background feature from the Z-DMP load had to be addressed. The spatially integrated intensity vs diffraction angle from the SCDI diagnostic without ZBL generated x-rays (Z3396) is shown in Figure 3-10. Although this null XRD data could be applied to all three Z-XRD experiments to deconvolve their x-ray backgrounds, an obvious caveat should be observed. Each of the three Z-XRD experiments had slightly different experimental parameters, such as Marx-charge voltages, flyer impact velocities, Z-DMP load geometry, and SCDI configuration, compared to the null experiment Z3396. The experimental parameters of Z3362 were the best match to those of Z3396, thus Rietveld refinement was used to analyze quantitatively the shock-compressed XRD results of Z3362.

3.2.3. Rietveld refinement

The Rietveld method [53] refines parameters to minimize the difference between an experimental pattern and a hypothesized model based on the crystal structure and instrumental parameters. The key fact is that the entire diffraction pattern, and not just line position, acts as a collection of observations. Using the Rietveld method, we model a multivariable structure-background-profile model to experimental data. We describe the crystal structure with: space group, lattice parameters, atomic positions, atomic site occupancies, atomic thermal parameters. The instrument is described by: a background, peak profile parameters and error correcting parameters. We also take into account that the x-ray emission of Mn is not monochromatic, but composed of 4 energies spanning 54 eV [54], and we model the emission profile accordingly.

Figure 3-11 illustrates the Rietveld full profile structural refinement of (a) XRD data as at ambient conditions prior to the shot as well as (b) XRD data obtained during Z3362. The pattern

measured *in situ*, during Z shot 3362 (Figure 3-11(b)), is composed of 2 reflections of un-shocked Be and 3 reflections of shocked Be. Both unshocked and shocked Be patterns are consistent with a hcp lattice. The diffraction angle coverage was selected to favor measurement of the shocked diffraction lines. The refinement also indicates about 68 wt.% of un-shocked Be and 32 ± 6 wt.% of shocked Be. This is consistent with measurements of velocimetry: 30% of shocked sample at the moment when the ZBL laser was fired, generating the x-ray beam. In summary, the Z-XRD experiment Z3362 showed that shocked-compressed Be, up to 182 GPa, is still in the hcp phase.

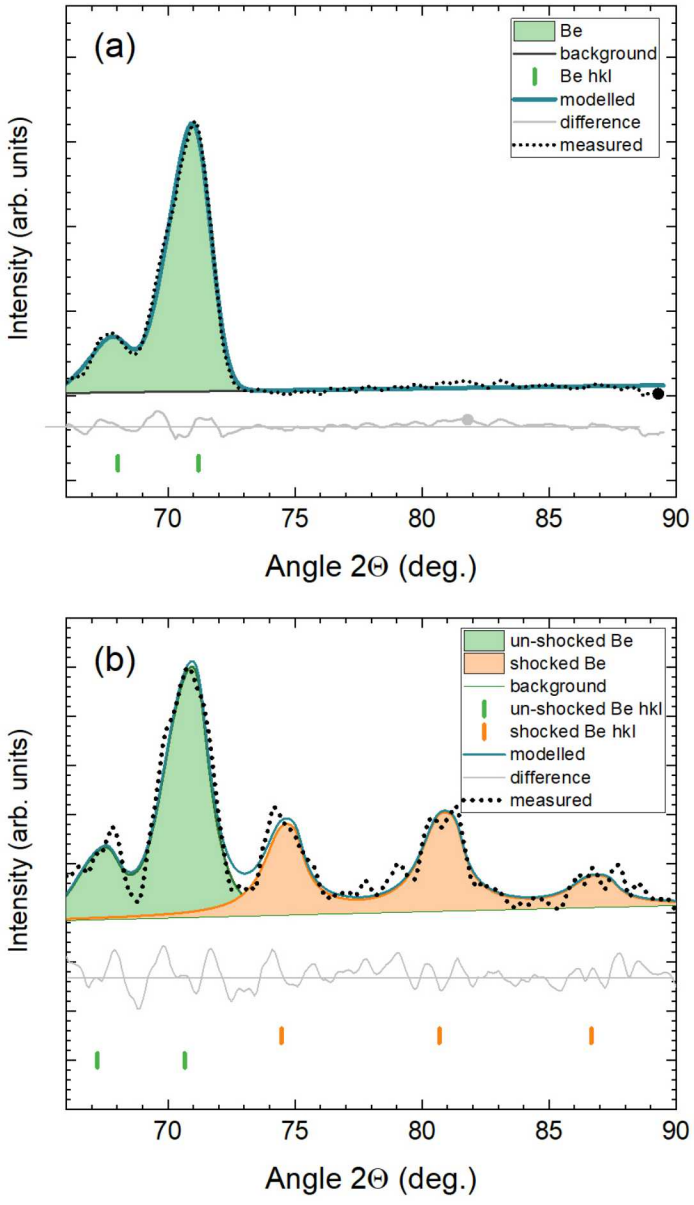

Figure 3-11. Rietveld refinement of XRD data for Z3362: (a) pre-shot, and (b) during Z-XRD experiment after removal of x-ray background from null shot Z3396. Short vertical lines are Miller indices of un-shocked and shocked Be.

4. NEXT STAGE DEVELOPMENTS

4.1. Stage 1: Near-term wrap-up

4.1.1. Improvements to the SCDI diagnostic

After successfully obtaining XRD data from dynamically compressed matter on Z using the SCDI diagnostic, several improvements could be implemented. First, the x-ray background emitting from the Z-DMP load needs to be suppressed further. If our hypothesis is correct and the crystal is imaging the hot A-K gap plasma, the geometry can be changed and additional shielding can be implemented. For example, the Z-DMP load assembly that surrounds the Be samples is typically made of aluminum, which is relatively transparent to x-rays. By fabricating the load assembly out of a higher-Z material such as copper, the emission from the hot temperature plasma in the A-K gap can be better attenuated. In addition, coating the impact side of the anode flyer plate with a thin layer of high-Z material (e.g. gold, platinum) could further shield the A-K gap x-ray emission. Additionally, the relative angle between the cathode stalk and the SCDI crystal can be changed or even flipped by 180° to move the bright x-ray emission zone out of the shifted diffraction pattern.

Furthermore, by cutting a narrow strip out of the IP, a linear diode array (LDA) detector could be simultaneously fielded with it inside the SCDI housing. The LDA would provide a time-resolved signal along with the IP's time-integrated image of the XRD pattern.

4.1.2. Limitations of the SCDI diagnostic

There are several features of the SCDI diagnostic that limit its viability to meet the long-term goals of Z-XRD. First, only x-rays at relatively low photon energy (4-10 keV) are viable with the current SCDI scheme. For higher photon energies (> 10 keV), higher reflection orders ($n > 4$) of the spherical HOPG crystal are required, whose reflection efficiency decreases accordingly. Second, the SCDI's sagittal focusing and the relatively poor imaging quality of HOPG crystals smear out any mesoscale features in the XRD patterns (e.g. grain size, preferred orientations). While the latter can be improved by using better-quality crystals such as Ge or Si crystals, crystal imaging above 10 keV appears infeasible due to the low integrated reflectivity of these crystals [31]. Therefore, in the mid-to-long-term plans we will switch to a different x-ray detection technology.

4.2. Stage 2: Mid-term plan

4.2.1. X-ray source

Two of the main goals of the Z-XRD project's Stage 2 are to increase x-ray flux and photon energy. Since single-shot XRD requires both sufficient photon energy and fluence, the laser generated x-ray source for Z-XRD will require improvement. The recent LDRD project 191235 investigated the use of a short-pulse laser to generate x-rays for XRD [55], and some of its results are reviewed in this section. First, the number of photons N_{photon} produced by a laser-irradiated target can be described as,

$$N_{photon} = \eta \frac{E_{laser}}{E_{photon}}, \qquad (6)$$

where E_{laser} is by the energy of the laser, E_{photon} is the photon energy of the x-ray, and η is the laser-to-x-ray conversion efficiency. Figure 4-1 shows the measured conversion efficiencies into 4π of the long-pulse ZBL and short-pulse Z-Petawatt (ZPW) lasers, as well as literature data of other short-pulse lasers [56], for various x-ray targets and corresponding x-ray photon energies. The blue data

show the rapid drop off for the long-pulse laser. While the green and pink data for the short-pulse laser (at different irradiances) show much more gradual decrease in conversion efficiency for higher photon energies. For example, the long pulse ZBL laser can produce 10^{15} photons of Mn-He$_\alpha$ 6.2 keV x-rays in 4π, but only 10^{12} photons of Zr-He$_\alpha$ 16 keV x-rays. Alternatively, the short-pulse ZPW laser can produce 10^{14} photons of Zr-K$_\alpha$ 16 keV x-rays. Overall, below 10 keV x-ray energy, ZBL is superior to ZPW, but above 10 keV, the ZPW laser is more efficient.

We plan to utilize the short-pulse ZPW laser system on Z to more efficiently generate x-rays with energies around 15-20 keV for XRD. The ZPW laser is currently undergoing an upgrade to full aperture, which will enable short-pulse laser experiments at 1–2 kJ laser energy. By using an off-axis parabolic mirror in final optics assembly (FOA) on Z and the Chama chamber, ZPW will be able to operate in a very large range of intensities from below 10^{16} W/cm^2 up to 10^{20} W/cm^2. This will help determining the optimum laser intensity, which balances K$_\alpha$ generation efficiency and background generation.

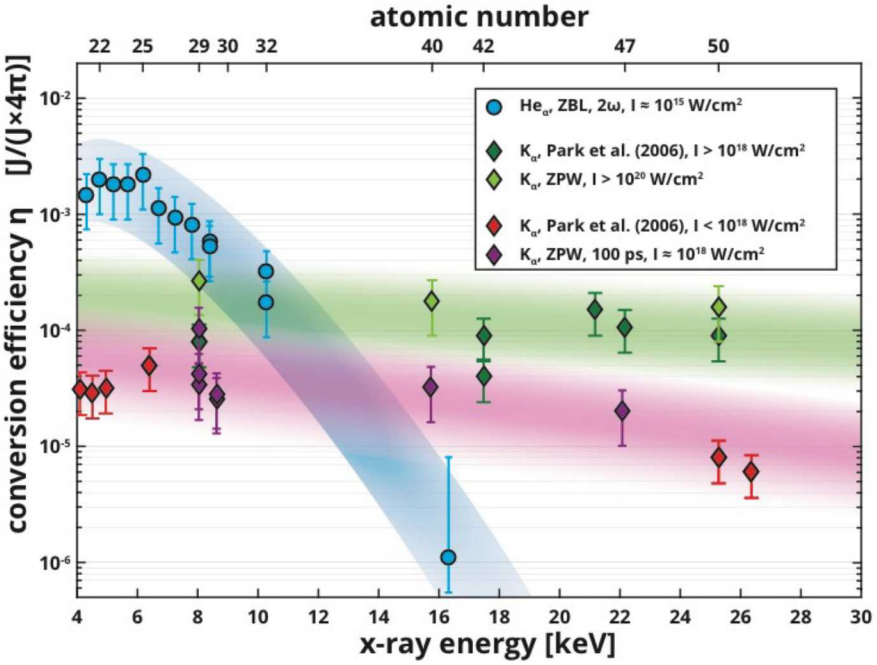

Figure 4-1. Comparison of laser-to-x-ray conversion efficiencies for long and short pulse lasers.

4.2.2. X-ray polycapillary lens

Typically, pinholes are used to collimate x-rays generated by laser-irradiated targets for XRD, which is very inefficient. We have examined x-ray optics, specifically x-ray polycapillary lenses (XPL), to improve the delivery of the x-rays to the sample [57]. Briefly, XPL consist of a bent array of 5–10 μm diameter hollow glass fibers in a hexagonal configuration, as shown in Figure 4-2. The x-rays are guided inside the hollow capillaries by the process of total external reflection at the boundary between vacuum and the inside glass surface.

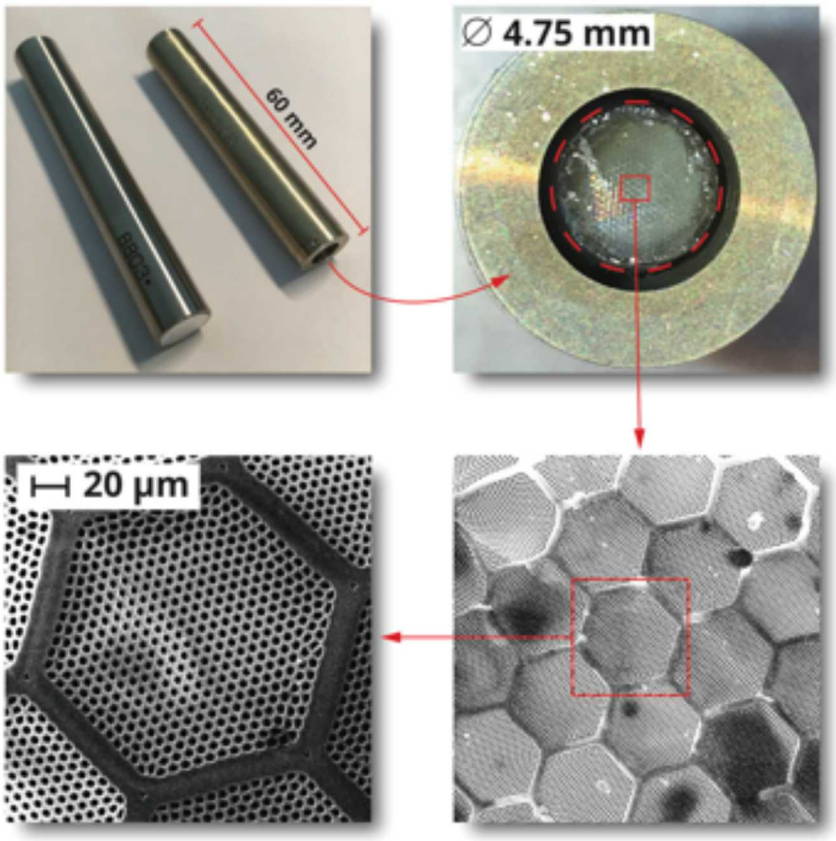

Figure 4-2. Photos and microscope images of an x-ray polycapillary lens.

Compared to a pinhole, it has a gain in x-ray flux of ~ 100-1000 times, which enables delivery of 10^9-10^{12} photons onto a sample. In the LDRD project 191235, we have compared the ambient XRD patterns measured using a pinhole collimator and with an XPL ([58], [59]). Figure 4-3 shows the XRD patterns of ambient Be using ZBL-generated Cu-He$_\alpha$ 8.4 keV x-rays. The left image of Figure 4-3(b) was obtained using a 1-mm diameter Ta pinhole. The right image was obtained using XPL, where the diffraction lines are brighter and better resolved.

For the mid-term Z-XRD scheme, XPL will be used to more efficiently collect x-rays emitted from the laser-driven source and to guide a collimated x-ray beam to the XRD sample. Using a collimated x-ray beam for XRD instead of the strongly-divergent x-ray pulse from a laser source will allow us to field an x-ray converter (described in the next section) much closer to the load compared to SCDI for enhanced XRD signal amplitudes without sacrificing resolution.

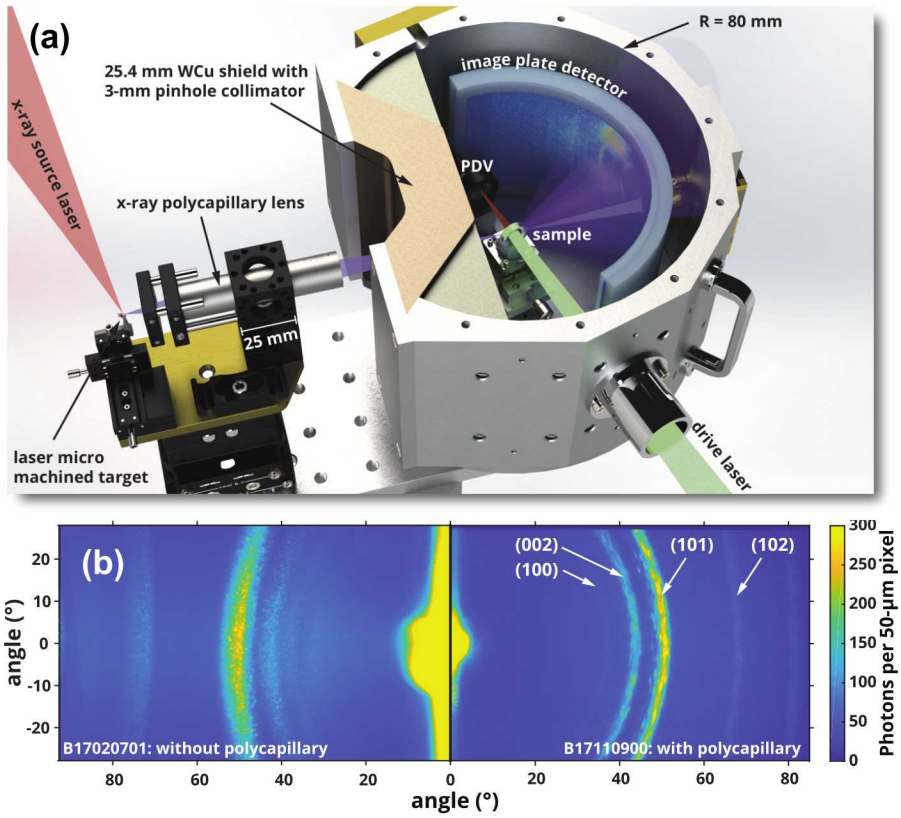

Figure 4-3. (a) Testing of x-ray polycapillary lens with ZBL and ambient Be sample. (b) XRD patterns without and with an x-ray polycapillary lens.

4.2.3. X-ray detection

The long-term detector scheme will require conversion of the diffracted x-rays to optical light, which will be transported away from the Z-DMP load and measured on and a fast-gated camera, or a diode array coupled to a digitizer array. This scheme will incorporate time-gating to allow measurement only during the short time window of the laser-generated x-ray pulse in which XRD occurs. This in turn will significantly reduce the unwanted background from the Z-DMP load. In this so-called Diffraction Scintillator Optic (DISCO), the scintillator is coupled to an optical imaging relay system (e.g. open beam optics or imaging fiber bundle). An assortment of scintillators could be used in the DISCO, which have various decay times, emission wavelengths, and light yield (see Table 4-1). For now, the P47 phosphor seems like a good initial scintillator to use because of its high light yield and acceptable decay time.

For the fast-gated camera, we are considering the Ultrafast X-ray Imager (UXI) camera [60]. It is based on a hybrid-CMOS chip that has been developed at Sandia. The camera is capable of acquiring 1 ns, time-gated, multi-frame image sets for HED physics experiments. One of the key reasons that makes the UXI camera suitable for Z-XRD is that it has been actively fielded on Z for x-ray backlighting since 05/2018, and has been shown to be robust to Z's EMP. Figure 4-4 shows a possible Z-XRD configuration using open beam optics and visible UXI camera (DISCO-UXI). The scintillator is placed near the Z-DMP load, a set of optics is used to image relay the XRD pattern onto

the UXI camera. Table 4-2 shows how the diffraction angle range, angular resolution, and signal level can be controlled by varying the scintillator distance from the sample.

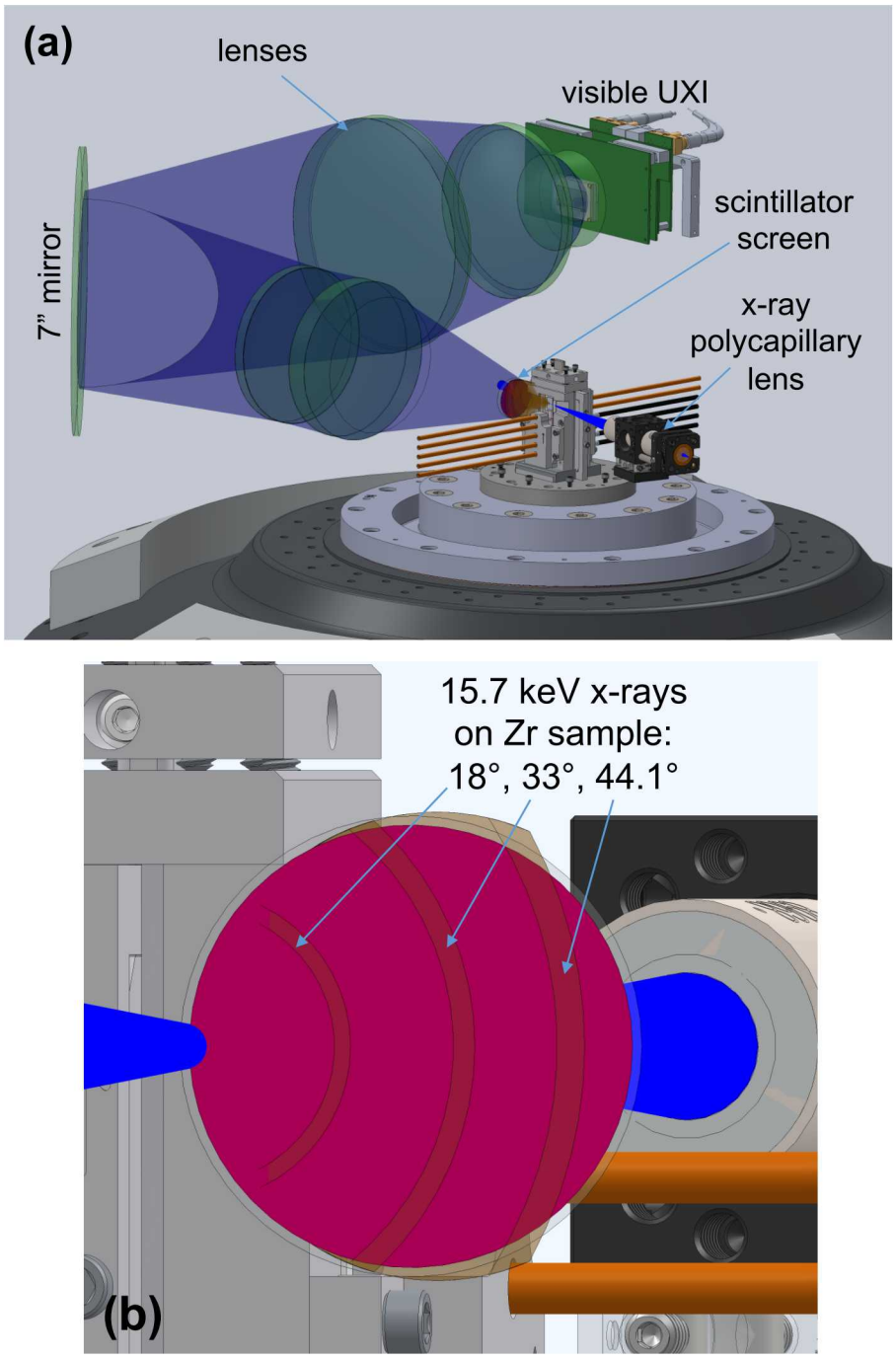

Figure 4-4. DISCO-UXI: (a) Possible Z-XRD configuration using an x-ray polycapillary lens, a scintillator screen, open beam optics, and a visible UXI camera. (b) Detail view of XRD pattern on a 1" diameter scintillator screen.

For the case when the Z experiment needs to be completely contained, the open beam optics will need to be replaced by imaging fibers. For example, there are high spatial resolution PMMA imaging fiber bundles that are readily available (e.g. Asahi Multi-core POF MBL-2000-24). To obtain reasonable coupling efficiency, a super-bundle of 7 registered imaging fibers could be used. Figure 4-5 shows a possible Z-XRD configuration with the DISCO-Fiber scheme. Compared to the DISCO-UXI, the optics are much reduced in size and cost. The diffraction signal level would decrease by a factor of ~100, but it should still remain reasonable for the measurement.

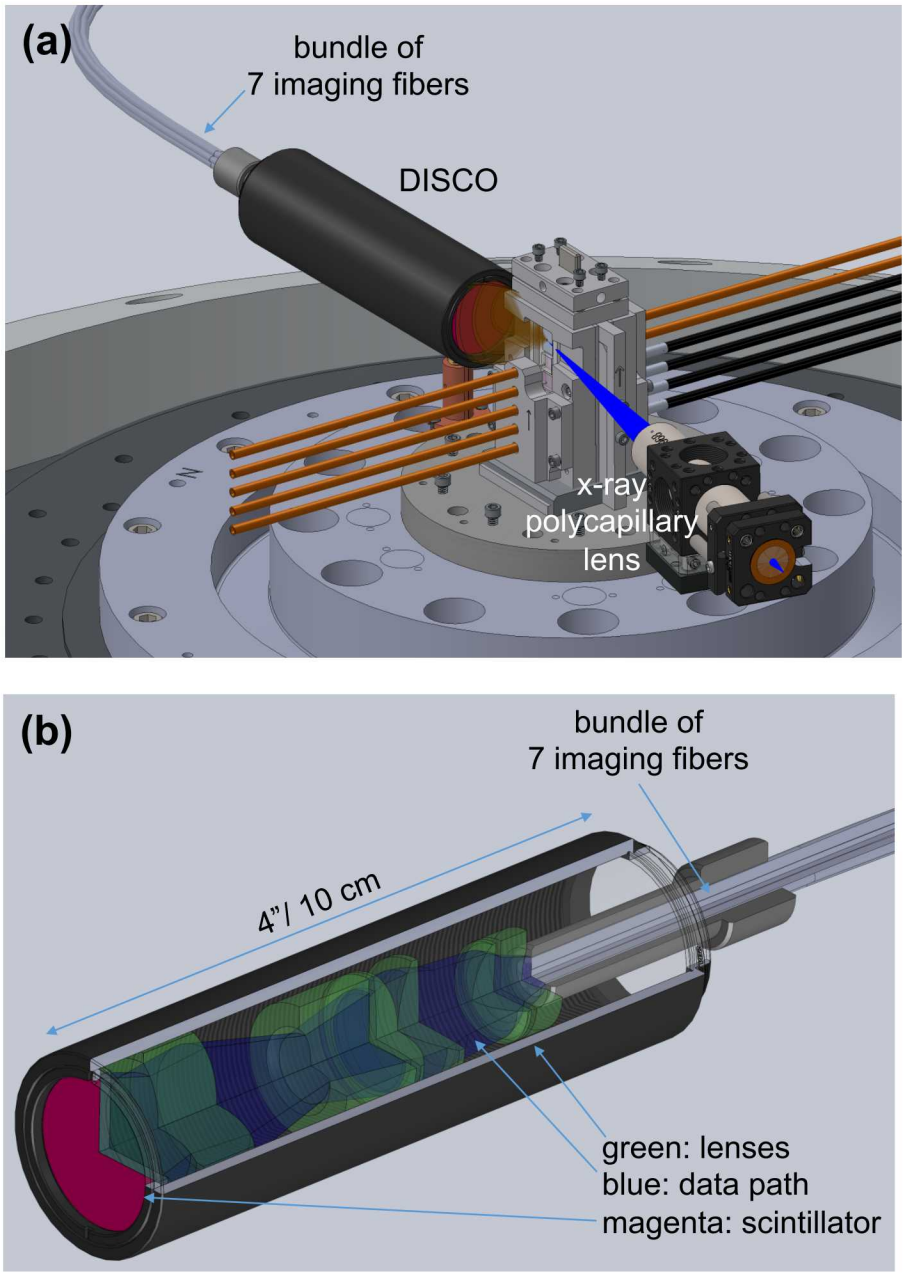

Figure 4-5. DISCO-Fiber: (a) Possible Z-XRD configuration using an x-ray polycapillary lens, a scintillator screen, and bundle of imaging fibers. (b) Internal view of lens focusing data into imaging fibers.

Table 4-1. Possible scintillators for DISCO.

Scintillator	Chemical Formula	1/e Decay Time (ns)	Emission Wavelength (nm)	Light Yield (photons/keV)
Mirrored P47	Gd_2O_2S:Tb	1000	550	95
Mirrored P43	Y_2SiO_3:Ce	70	400	38
Exalite 404	$C_{50}H_{58}$	3	400	-
LSO	Lu_2SiO_5:Ce^{3+}	47	400	30
PreLude420	$Lu_{1.8}Y_2SiO_5$:Ce	41	420	32
BriLanCe380	$LaBr_3$:Ce	16	380	63
ZnO:Ga	ZnO:Ga	0.8	385	9
ScintiFast	-	< 1	390	7.5
R42	-	68	510	11

Table 4-2. DISCO configuration parameters.

Scintillator Distance (mm)	Diffraction Range $\Delta\phi(^\circ)$	Diffraction Angle Resolution $\delta\phi(^\circ)$	Signal for 8 keV (counts)		Signal for 17.4 keV (counts)	
			UXI	Fiber	UXI	Fiber
45.8	30.5	0.1	5×10^6	4.6×10^4	1×10^5	1.1×10^3
25.4	**52**	**0.18**	$\mathbf{1 \times 10^7}$	$\mathbf{1.5 \times 10^5}$	$\mathbf{4 \times 10^5}$	$\mathbf{4 \times 10^3}$
18.3	69	0.25	3×10^7	2.8×10^6	8×10^5	7.3×10^3

4.3. Stage 3: Long-term plan

In the long term, we plan to implement an XRD setup for Z experiments that require a dedicated containment vessel. Figure 4-6 presents the conceptual design of a Z-XRD containment experiment that leverage the experience gained in Stages 1 and 2.

The short-pulse ZPW laser will irradiate an x-ray target to generate > 15 keV x-rays. An XPL developed in Stage 2 will be used to collect and inject x-rays through small (< 1cm diameter) entrance ports, covered with x-ray windows, in the walls of the containment vessel. After the x-rays have been directed onto a dynamically compressed high-Z sample mounted to the Z-DMP load, the x-ray ports will be rapidly sealed. Also, inside the containment vessel, x-ray detection will be performed with the DISCO x-ray-to-optical converter developed in Stage 2. The converted optical data will be transported within an isolated medium (e.g. imaging fiber bundle) to a data recording unit outside of the containment vessel.

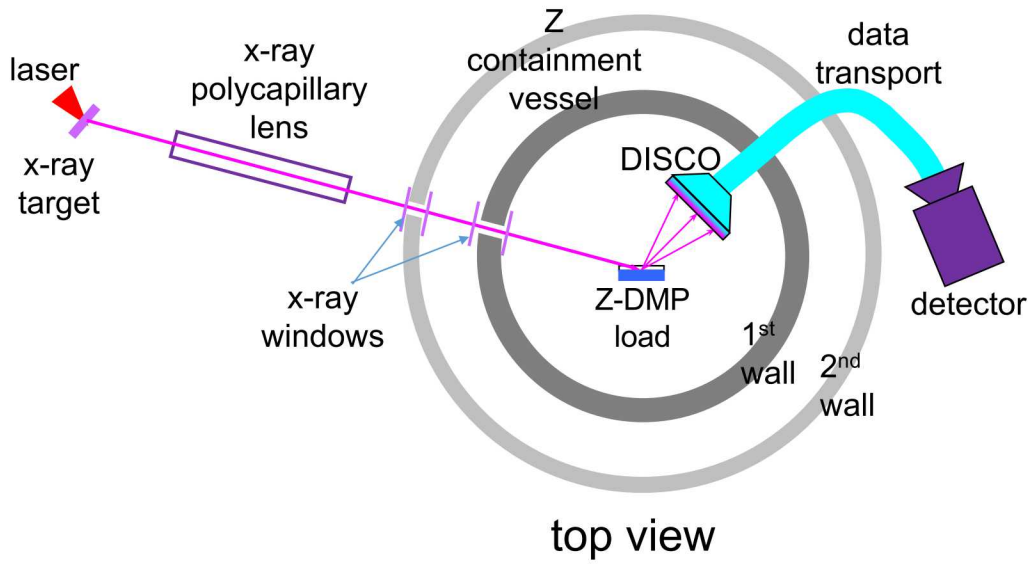

Figure 4-6. Conceptual design for Z-XRD containment experiment.

5. SUMMARY

The overall goal of the Z-XRD Project is to develop an x-ray diffraction (XRD) capability to diagnose the lattice parameters and crystal structures of shock- and ramp-compressed samples on Z-DMP experiments. A three-stage strategy has been developed for the Z-XRD Project. This report primarily presented the recent experimental results that demonstrated the successful completion of Stage 1. A brief overview of the groundwork for Stages 2 and 3 of the Z-XRD Project was also described.

In Stage 1, the new spherical crystal diffraction imager (SCDI) diagnostic was implemented on the Z-accelerator. Several Z-XRD experiments were performed in which the SCDI diagnostic measured the XRD patterns of beryllium (Be) samples that had been shock-compressed on Z-Dynamic Material Properties (DMP) loads. Specifically, the Z-Beamlet laser generated 6.2 keV x-rays to probe the shock-compressed Be states (1.8-2.2 Mbar). The diffracted x-rays from the shocked Be sample were collected by the SCDI diagnostic's spherical HOPG (highly oriented pyrolytic graphite) crystal, and focused onto an image plate detector fielded inside an 1"-thick tungsten-walled housing, which protected the data from the Z-DMP load's destructive debris field. The measured SCDI data consisted of XRD patterns from both the Be sample's ambient and shocked states, and x-ray background from the Z-DMP load. Through quantitative characterization of the Z-DMP load x-ray emission, the XRD data from the shocked state of Be was revealed. While the SCDI scheme has been shown to be a viable XRD diagnostic for low-Z materials, the long-term goal of XRD of higher-Z materials require switching to a new scheme.

Multiple developments are underway to meet the mid-term goals of Stage 2. First, the short pulse Z-Petawatt laser will be upgraded and implemented onto Z. This will enable higher photon energy (> 15 keV) x-rays to be generated for Z-XRD experiments. Second, an x-ray polycapillary lens will be used to significantly increase the x-ray flux onto the Z-XRD sample. Third, a new x-ray detection scheme involving the conversion of x-rays to optical light will enable time-gated measurements of the Z-XRD data. Finally, the new Z-XRD scheme developed in Stage 2 will be implemented on Z-containment experiments in Stage 3.

REFERENCES

[1] M. K. Matzen, M. A. Sweeney, R. G. Adams, J. R. Asay, J. E. Bailey, G. R. Bennett, D. E. Bliss, D. D. Bloomquist, T. A. Brunner, R. B. Campbell, G. A. Chandler, C. A. Coverdale, M. E. Cuneo, J. P. Davis, C. Deeney, M. P. Desjarlais, G. L. Donovan, C. J. Garasi, T. A. Haill, C. A. Hall, D. L. Hanson, M. J. Hurst, B. Jones, M. D. Knudson, R. J. Leeper, R. W. Lemke, M. G. Mazarakis, D. H. McDaniel, T. A. Mehlhorn, T. J. Nash, C. L. Olson, J. L. Porter, P. K. Rambo, S. E. Rosenthal, G. A. Rochau, L. E. Ruggles, C. L. Ruiz, T.W. L. Sanford, J. F. Seamen, D. B. Sinars, S. A. Slutz, I. C. Smith, K. W. Struve, W. A. Stygar, R. A. Vesey, E. A. Weinbrecht, D. F. Wenger, and E. P. Yu, Phys. Plasmas **12**, 055503 (2005).

[2] R. W. Lemke, M. D. Knudson, D. E. Bliss, K. Cochrane, J.-P. Davis, A. A. Giunta, H. C. Harjes, and S. A. Slutz, J. Appl. Phys. **98**, 073530 (2005).

[3] M. D. Knudson, M. P. Desjarlais, and D. H. Dolan, Science **322**, 1822 (2008).

[4] K. R. Cochrane, R. W. Lemke, Z. Riford, and J. H. Carpenter, J. Appl. Phys. **119**, 10 (2016).

[5] T. R. Mattsson, J. M. D. Lane, K.R. Cochrane, M. P. Desjarlais, A. P. Thompson, F. Pierce, and G. S. Grest, Phys. Rev. B **81**, 9 (2010)

[6] S. Root, L. Shulenburger, R. W. Lemke, D. H. Dolan, T.R. Mattsson, and M. P. Desjarlais, Phys. Rev. Lett. **115**, 198501 (2015).

[7] M. D. Knudson, R. W. Lemke, D. B. Hayes, C. A. Hall, C. Deeney, J. R. Asay, J. Appl. Phys. **94**, 4420 (2003).

[8] C. A. Hall, J. R. Asay, M. D. Knudson, W. A. Stygar, R. B. Spielman, T. D. Pointon, D. B. Reisman, A. Toor, and R. C. Cauble, Rev. Sci. Instrum. **72**, 3587 (2001).

[9] J.-P. Davis, C. Deeney, M. D. Knudson, R. W. Lemke, T. D. Pointon, and D. E. Bliss, Phys. Plasmas **12**, 056310 (2005).

[10] C. T. Seagle, J.-P. Davis, M. D. Knudson, J. Appl. Phys. **120,** 165902 (2016).

[11] L. M. Barker and R. E. Hollenbach, J. Appl. Phys. **43**, 4669 (1972).

[12] O. T. Strand, D. R. Goosman, C. Martinez, T. L. Whitworth, and W. W. Kuhlow, Rev. Sci. Instrum. **77**, 083108 (2006).

[13] P. Kalita, P. Specht, S. Root, N. Sinclair, A. Schuman, M. White, A. L. Cornelius, J. Smith, S. Sinogeikin, Phys. Rev. Lett. **119**, 255701 (2017).

[14] D. Kraus, A. Ravasio, M. Gauthier, D. O. Gericke, J. Vorberger, S. Frydrych, J. Helfrich, L. B. Fletcher, G. Schaumann, B. Nagler, B. Barbrel, B. Bachmann, E. J. Gamboa, S. Gode, E. Granados, G. Gregori, H. J. Lee, P. Neumayer, W. Schumaker, T. Doppner, R. W. Falcone, S. H. Glenzer, and M. Roth, Nature Communications **7**, 10970 (2016).

[15] C. Kittel and P. McEuen, Introduction to Solid State Physics, 8th Edition (John Wiley & Sons, Inc, 1996), ISBN 0-471-41526-x.

[16] D. C. Swift, Rev. Sci. Instrum. **79**, 013906 (2008).

[17] D. H. Kalantar, E. Bringa, M. Caturla, J. Colvin, K. T. Lorenz, M. Kumar, J. Stolken, A. M. Allen, K. Rosolankova, and J. S. Wark, M. A. Meyers, M. Schneider, and T. R. Boehly Rev. Sci. Instrum. **74**, 1929 (2003).

[18] M. Suggit, G. Kimminau, J. Hawreliak, B. Remington, N. Park, and J. Wark, Rev. Sci. Instrum. **81**, 083902 (2010).

[19] P. A. Rigg and Y. M. Gupta, J. Appl. Phys. **93**, 3291 (2003).

[20] B. J. Jensen and Y. M. Gupta, J. Appl. Phys. **104**, 013510 (2008).

[21]J. R. Rygg, J. H. Eggert, A. E. Lazicki, F. Coppari, J. A. Hawreliak, D. G. Hicks, R. F. Smith, C. M. Sorce, T. M. Uphaus, B. Yaakobi, and G. W. Collins, Rev. Sci. Instrum. **83**, 113904 (2012).

[22]J. Eggert, D. Braun, R. Rygg, A. Lazicki, D. Fratanduono, R. Smith, F. Coppari, R. Kraus, D. Swift, J. McNaney, Y. Ping, K. Blobaum, M. Wilson, M. Ahmed, G. Collins, and T. Arsenlis, Bulletin of the American Physical Society **60**, H5.6 (2015).

[23]A. E. Gleason, C. A. Bolme, E. Galtier, H. J. Lee, E. Granados, D. H. Dolan, C. T. Seagle, T. Ao, S. Ali, A. Lazicki, D. Swift, P. Celliers, and W. L. Mao, Phys. Rev. Lett. **119**, 025701 (2017).

[24]S. J. Turneaure, S. M. Sharma, and Y. M. Gupta, Phys. Rev. Lett. **121**, 135701 (2018).

[25]D. B. Sinars, G. R. Bennett, D. F. Wenger, M. E. Cuneo, D. L. Hanson DL, J. L. Porter, R. G. Adams, P. K. Rambo, D. C. Rovang, and I. C. Smith, Rev. Sci. Instrum. **75**, 3672 (2004).

[26]G. R. Bennett, D. B. Sinars, D. F. Wenger, M. E. Cuneo, R. G. Adams, W. J. Barnard, D. E. Beutler, R. A. Burr, D. V. Campbell, L. D. Claus, J. S. Foresi, D. W. Johnson, K. L. Keller, C. Lackey, G. T. Leifeste, L. A. McPherson, T. D. Mulville, K. A. Neely, P. K. Rambo, D. C. Rovang, L. E. Ruggles, J. L. Porter, W. W. Simpson, I. C. Smith, and C. S. Speas, Rev. Sci. Instrum. **77**, 10E322 (2006).

[27]M. S. Schollmeier, M. Geissel, J. E. Shores, I. C. Smith, and J. L. Porter, Appl. Opt. **54**, 5147 (2015).

[28]D. B. Sinars, G. A. Chandler, J. E. Bailey, R. C. Mancini, G. A. Rochau, D. F. Wenger, R. G. Adams, M. L. Adams, H. A. Scott, A. Ya. Faenov, T. A. Pikuz, and S. A. Pikuz, J. Quant. Spectrosc. Radiat. Trans. **99**, 595 (2006).

[29]E. C. Harding, T. Ao, J. E. Bailey, G. Loisel, D. B. Sinars, M. Geissel, G. A. Rochau, and I. C. Smith, Rev. Sci. Instrum. **86**, 043504 (2015).

[30]W.H. Bragg and W.L. Bragg, Proceedings of the Royal Society of London. Series A, Containing Papers of a Mathematical and Physical Character **88**, 428 (1913).

[31]M. S. Schollmeier and G. P. Loisel, RSI **87**, 123511 (2016).

[32]T. Ao, E. C. Harding, J. E. Bailey, G. Loisel, S. Patel, D. B. Sinars, L. P. Mix, and D. F. Wenger, J. Quant. Spectrosc. Radiat. Transf. **144**, 92 (2014).

[33]L. E. Ruggles, J. L. Porter, P. K. Rambo, W. W. Simpson, M. F. Vargas, G. R. Bennett, and I. C. Smith, Rev. Sci. Instrum. **74**, 2206 (2003).

[34]Y. Amemiya and J. Miyahara, Nature **336**, 89 **(**1988).

[35]S. G. Gales and C. D. Bentley, Rev. Sci. Instrum. **75**, 4001 (2004).

[36]A. L. Meadowcroft, C. D. Bentley, and E. N Scott, Rev. Sci. Instrum. **79**,113102 (2008).

[37]B. R. Maddox, H. S. Park, B. A. Remington, N. Izumi, S. Chen S, et al. Rev. Sci. Instrum. **82**, 82:023111 (2011).

[38]M. J. Berger, J. H. Hubbell, S. Seltzer, J. Chang, J. S. Coursey, R. Sukumar, D. S. Zucker, and K. Olsen, XCOM: Photon Cross Sections Database, NIST (2018), https://www.nist.gov/pml/xcom-photon-cross-sections-database.

[39]D. H. Dolan, T. Ao, and S. C. Grant, Sandia Report, SAND2016-6848, August 2016.

[40]Nanophorm LLC, Incline Village, NV, USA.

[41]Optigraph GmbH, Berlin, Germany.

[42]G. I. Kerley, Sandia Report, SAND2003-3784, October 2003.

[43]K. L. Wilson, R. A Causey, W. L. Hsu, B. E. Mills, M. F. Smith, and J. B. Whitley, J. Vac. Sci. Technol. A **8**, 1750 (1990).

[44]K. Kadas, L. Vitos, B. Johansson, and J. Kollar, Phys. Rev. B **75**, 035132 (2007).

[45]K. Nakano, Y. Akahama, and H. Kawamura, J. Phys.: Condens. Matter **14**, 10569 (2002).

[46]F. Luo, L.-C. Cai, X.-R. Chen, F.-Q. Jing, and D. Alfe, J. Appl. Phys. **111**, 053503 (2012).

[47]G. Robert, P. Legrand, and S. Bernard, Phys. Rev. B **82**, 104118 (2010).

[48]L. X. Benedict, T. Ogitsu, A. Trave, C. J. Wu, P. A. Sterne, and E. Schwegler, Phys. Rev. B **79**, 064106 (2009).

[49]M. Francois and M. Contre, in *Conference Internationale sur la Metallurgie du Beryllium* (Universite de France, Grenoble, Paris, 1965).

[50]A. Abey, Lawrence Livermore National Laboratory Report No. UCRL-53567, 1991.

[51]W. J. Evans, M. J. Lipp, H. Cynn, C. S. Yoo, M. Somayazulu, D. Häusermann, G. Shen, and V. Prakapenka, Phys. Rev. B **72**, 094113 (2005).

[52]A. Lazicki, A. Dewaele, P. Loubeyre, and M. Mezouar, Phys. Rev. B **86**, 174118 (2012).

[53]H. M. Rietveld, J. Appl. Crystallogr. **2**, 65 (1969).

[54]J. E. Bailey, T. Ao, E. Harding, S. B. Hansen, M. P. Desjarlais, R.W. Lemke, G. A. Rochau, J. Reneker, and D. Romero, Sandia Report, SAND2012-7998, September 2012.

[55]M. Schollmeier, T. Ao, E. S. Field, B. R. Galloway, P. Kalita, M. W. Kimmel, D. V. Morgan, P. K. Rambo, J. Schwarz, J. E. Shores, I. C. Smith, C. S. Speas, J. F. Benage, and J. L. Porter, Sandia Report, SAND2018-10612, September 2018.

[56]H.-S. Park, D. M. Chambers, H. K. Chung, R. J. Clarke, R. Eagleton, E. Giraldez, T. Goldsack, R. Heathcote, N. Izumi, M. H. Key, et al., Physics of Plasmas **13**, 056309 (2006).

[57]M. Schollmeier, T. Ao, E. S. Field, B. R. Galloway, P. Kalita, M. W. Kimmel, D. V. Morgan, P. K. Rambo, J. Schwarz, J. E. Shores, I. C. Smith, C. S. Speas, J. F. Benage, and J. L. Porter, Rev. Sci. Instrum. **89**, 10F102 (2018).

[58]XOS, East Greenbush, NY, USA.

[59]Helmut Fischer GmbH, Institut für Elektronik und Messtechnik, Berlin, Germany.

[60]L. Claus, A. Boone, T. England, L. Fang, Q. Looker, B. B. Mitchell, A. Montoya, J. L. Porter, M. Sanchez, A. J. Vigil, E. R. Hurd, A. Carpenter, M. Dayton, C. E. Durand, and G. Rochau, Proc. SPIE **10763**, 107630M (2018).

DISTRIBUTION

Email—Internal

Name	Org.	Sandia Email Address
Dan Sinars	1600	dbsinar@sandia.gov
Michael Desjarlais	1600	mpdesja@sandia.gov
John Benage	1640	jfbenag@sandia.gov
Dawn Flicker	1640	dgflick@sandia.gov
Kyle Cochrane	1641	kcochra@sandia.gov
Heath Hanshaw	1641	hlhansh@sandia.gov
Andrew Porwitzky	1641	ajporwi@sandia.gov
Luke Shulenburger	1641	lshulen@sandia.gov
Joshua Townsend	1641	jptowns@sandia.gov
Tommy Ao	1646	tao@sandia.gov
Brittany Branch	1646	babranc@sandia.gov
Justin Brown	1646	jlbrown@sandia.gov
Jean-Paul Davis	1646	jpdavis@sandia.gov
Dan Dolan	1646	dhdolan@sandia.gov
Sakun Duwal	1646	sduwal@sandia.gov
Sean Grant	1646	scgrant@sandia.gov
Patricia Kalita	1646	pekalit@sandia.gov
Marcus Knudson	1646	kdknuds@sandia.gov
Chad McCoy	1646	camccoy@sandia.gov
Seth Root	1646	sroot@sandia.gov
Christopher Seagle	1646	ctseagl@sandia.gov
Paul Specht	1646	pespech@sandia.gov
Jack Wise	1646	jlwise@sandia.gov
Gregory Rochau	1680	garocha@sandia.gov
Michael Jones	1681	micjone@sandia.gov
John Porter	1682	jlporte@sandia.gov
Patrick Rambo	1682	prambo@sandia.gov
Marius Schollmeier	1682	mscholl@sandia.gov
Jonathon Shores	1682	jeshore@sandia.gov
Ian Smith	1682	icsmith@sandia.gov
Christopher Speas	1682	csspeas@sandia.gov
Thomas Mattsson	1684	trmatts@sandia.gov

Name	Org.	Sandia Email Address
Paul Gard	1691	pdgard@sandia.gov
Caroline Blada	1692	cbblada@sandia.gov
James Williams	1692	jwilli6@sandia.gov
Technical Library	01177	libref@sandia.gov

Hardcopy—Internal

Number of Copies	Name	Org.	Mailstop
1	Patricia Kalita	1646	1106
1	Marius Schollmeier	1682	1192
5	Tommy Ao	1646	1195

This page left blank

Sandia National Laboratories

Sandia National Laboratories is a multimission laboratory managed and operated by National Technology & Engineering Solutions of Sandia LLC, a wholly owned subsidiary of Honeywell International Inc. for the U.S. Department of Energy's National Nuclear Security Administration under contract DE-NA0003525.